Deep-learning deconvolution and segmentation of fluorescent membranes for high-precision bacterial cell-size profiling

Octavio Reyes-Matte[1,*], Carsten Fortmann-Grote[1], Beate Gericke[1], Nadja Hüttmann[1], Nikola Ojkic[2], Javier Lopez-Garrido[1,*]

[1] Max Planck Institute for Evolutionary Biology, Plön, Germany

[2] School of Biological and Behavioral Sciences, Queen Mary University of London, UK

Correspondence: lopezgarrido@evolbio.mpg.de; reyesmatte@evolbio.mpg.de

Keywords: image segmentation, image deconvolution, bacterial cell size, PBP1, *Priestia megaterium*, *Bacillus*

ABSTRACT

Evolutionary studies in bacteria have emphasized genetic and metabolic diversity, while cell-size variation has received less attention. Here we introduce MEDUSSA, a high-throughput method for precise bacterial cell-size profiling based on automatic segmentation of fluorescent membrane images, well suited to studying cell-size diversity. The approach uses deep-learning-based membrane deconvolution, segmentation models fine-tuned for fluorescent-membrane images, and error-corrected cell measurement to extract accurate sizes from individual bacterial cells regardless of shape, size, chaining, or clustering. Our method overcomes limitations of phase-contrast segmentation, yielding reliable single-cell dimensions. We applied MEDUSSA to six strains of *Priestia megaterium* and found over twofold differences in cell volume across strains, largely driven by differences in cell width. We identified a partially-functional PBP1 allele that underlies the reduced width of one strain. Together, these results demonstrate the power of comparative analyses in bacterial cell biology and expand the toolkit to investigate the evolution of bacterial cell size.

INTRODUCTION

Bacterial cells are often perceived as uniformly small, which has led to a relative lack of attention to the evolution of bacterial cell size. Yet, careful microscopic observation has revealed an incredible diversity of bacterial shapes and sizes, with cell volumes spanning multiple orders of magnitude (Schavemaker & Munoz-Gomez, 2022; Schober et al., 2025). Even among closely related species, cell size can vary significantly. For instance, strains from two *Bacillus* species, *B. thuringiensis* and *B. pumilus*, can differ in volume by nearly an order of magnitude (Lopez-Garrido et al., 2018), suggesting that cell size is an evolvable trait capable of changing over relatively short evolutionary timescales.

Despite this diversity, our appreciation of bacterial cell size variation at finer evolutionary scales remains limited. Systematic studies have focused on mutant libraries in a few model strains (Juillot et al., 2021; Ursell et al., 2017). However, comparative studies analyzing the size of different bacterial strains or species are rare (Delaby et al., 2025; Gray et al., 2019), and most available data come from independent studies, often using different imaging methods and manual measurements of a few representative cells cultured in different conditions. While this highlights bacterial size diversity, methodological inconsistencies make cross-study comparisons difficult. As a result, we lack a clear picture of how bacterial cell size vary among closely related species and strains.

Recent advances in image analysis pose a unique opportunity for the standardization of methods to measure bacterial cell size and may help to address these challenges. In particular, the incorporation of machine-learning into image analysis pipelines have enabled the automatic identification and precise delineation of boundaries of individual bacterial cells in microscopy images. This process, known as image segmentation, generates masks of individual cells that can be used for accurate cell size measurements. The U-Net, a convolutional neural network architecture originally designed for the analysis of biomedical images (Falk et al., 2019; Ronneberger et al., 2015), is behind some of the most powerful image segmentation algorithms currently available, such as StarDist (Schmidt et al., 2018), DeLTA (Lugagne et al., 2020), Cellpose (Stringer et al., 2021), MiSiC (Panigrahi et al., 2021), Omnipose (Cutler et al., 2022), DeepBacs (Spahn et al., 2022) and DistNet (Ollion et al., 2024), to name a few. More recently, vision transformers (Dosovitskiy et al., 2020) have enabled the development of foundation models (Kirillov et al., 2023; Zou et al., 2023), which support strong off-the-shelf performance and facilitate fine-tuning on custom data.

Several models have leveraged large public microscopy datasets to achieve high flexibility, including microSAM (Archit et al., 2025), Cellpose-SAM (Pachitariu et al., 2025) and CellSAM (Marks et al., 2025). These tools are significantly improving the precision and automation of bacterial cell segmentation, paving the way for more consistent and reproducible cell size measurements.

Here, we have fine-tuned and benchmarked some these models for segmenting fluorescent membranes. Building on this, we developed a pipeline for extracting precise single-cell size information from fluorescent membrane images, which allows the characterization of individual cell sizes regardless of clustering or chaining patterns. We applied this pipeline, that we call MEDUSSA (MEmbrane DeconvolUtion and Segmentation for Size Analyses), to investigate cell-size diversity across six strains of *Priestia megaterium*, a Gram-positive bacterium commonly used for physiological studies and biotechnological applications (Logan & Vos, 2015). We found significant differences in volume between the strains—spanning more than twofold—underpinned by consistent differences in cell length and width. We further link width differences between two of the strains to a specific mutation in *ponA*, which encodes penicillin binding protein 1 (PBP1), resulting in a hypomorphic PBP1 allele.

RESULTS

Limitations of phase contrast segmentation for single cell studies.

Deep-learning-based segmentation algorithms are versatile and can segment different types of images, as long as they are trained with appropriately labeled datasets for the specific task. However, phase-contrast has become the default imaging modality for bacterial segmentation, as it provides excellent contrast between cells and background without the need for staining or genetic manipulation (Cutler et al., 2022; Ducret et al., 2016; O'Connor et al., 2022; Ollion et al., 2024; Paintdakhi et al., 2016; Stylianidou et al., 2016; Ursell et al., 2017; Van Valen et al., 2016). Despite its advantages, phase contrast images have limitations for cell size estimation. Firstly, they lack clear visual references to precisely define cell boundaries. Secondly, phase contrast does not allow the distinction of cells that remain attached after division, complicating the identification of individual cells in bacterial species that form cellular chains (Holt et al., 1994; Syvertsson et al., 2016). For instance, *Bacillus subtilis* and related species form heterogeneous populations in which single cells coexist with long chains consisting of dozens of cells (Kearns & Losick, 2005; Margulis et al., 1998). Because the separation of individual cells within a chain is not visible in phase-contrast images, state-of-the-art segmentation models optimized for phase-contrast segmentation, such as the Omnipose "bact_phase_omni" model (Cutler et al., 2022), segment chains as very long individual cells, making it difficult to extract information at the single cell level (Fig. 1a,c).

This issue can be circumvented by staining the cell membranes with lipophilic fluorescent dyes such as FM 4-64 (Pogliano et al., 1999) or Nile Red (Strahl et al., 2014), which allows the visualization of the septal membranes that separate individual cells within chains (Fig. 1b,d). The fluorescence intensity profile of FM 4-64-stained membranes shows a sharp peak that can be traced around the cell (Fig 1e,f), providing an unambiguous guide to delimit the cell boundaries. We therefore explored the performance of different segmentation models on fluorescent membrane images.

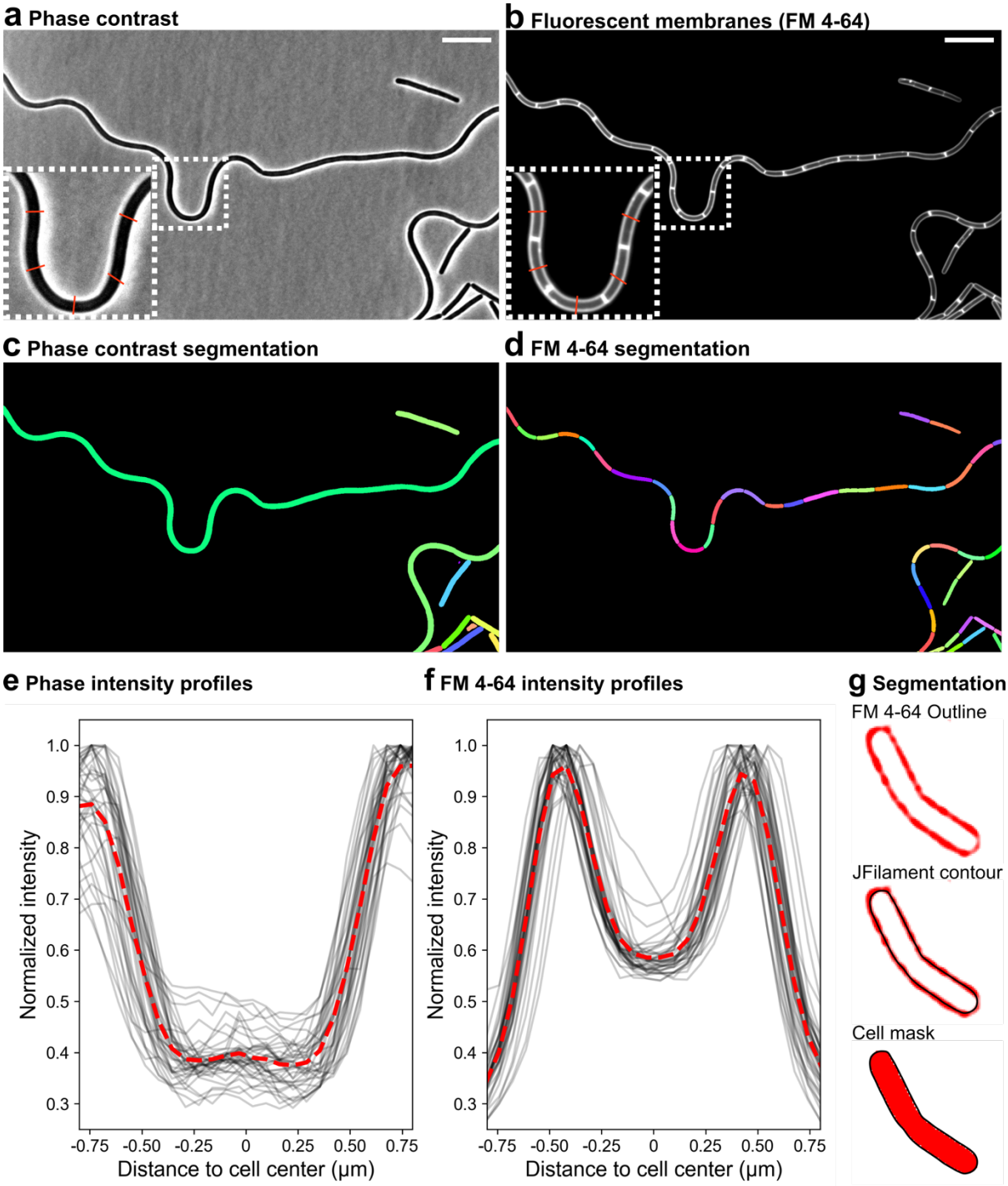

Figure 1. Phase-contrast versus fluorescent-membrane segmentation. a, **b**, Phase-contrast (**a**) and fluorescent membrane images (**b**) of *B. subtilis* growing vegetatively. Membranes were stained with FM 4-64. The insets show zoomed-in views of the boxed regions; the red lines illustrate the paths along which intensity profiles are calculated in panels **e** and **f**. **c**, **d**, Segmentation masks for the phase-contrast (**c**) and fluorescent membrane (**d**) images shown in **a** and **b**. The phase-contrast image was automatically segmented with Omnipose (Cutler et al., 2022) and the fluorescent-membrane image was manually segmented with JFilament (Smith et al., 2010) (see also panel **g**). Every mask has a different color. **e**, **f**, Phase-contrast (**e**) and fluorescent membrane (**f**) intensity profiles of 39 cells, measured along a 24-pixel line perpendicular to their long axis, centered at midcell (illustrated in insets in panels **a** and **b**). Pixel intensities were normalized to the maximum intensity observed across the lines for each imaging modality. **g**, Example of manual fluorescent-membrane segmentation using the active contour software JFilament (Smith et al., 2010).

High-throughput segmentation of fluorescent membranes.

We fine-tuned existing deep-learning segmentation models for segmenting fluorescent membrane images of bacterial cells, and benchmarked their performance. We focused on Cellpose3 (Stringer & Pachitariu, 2025), Omnipose (Cutler et al., 2022), and the SAM-based foundation models microSAM (Archit et al., 2025) and Cellpose-SAM (Pachitariu et al., 2025). Omnipose has been reported to perform better on elongated cells than other segmentation algorithms (Cutler et al., 2022). The models were fine-tuned using over seven-thousand FM 4-64-stained *B. subtilis* cells annotated with JFilament active-contour software (Fig. 1g) (Smith et al., 2010), which allows the semiautomated generation of snakes that track the fluorescent membrane peak around the cell, thereby diminishing user annotation bias. JFilament snakes precisely delimit cell contours and provide accurate cell dimensions (Supplementary Fig. 1). The training dataset included single cells, cells within chains and cells within clusters (see Methods for details). We tested the fine-tuned models with images of three bacilli of different sizes: *B. subtilis*, *B. thuringiensis*, and *Priestia megaterium* (Fig. 2a; Supplementary Fig. 2a). We also tested Morphometrics, a non-deep-learning segmentation method that has shown good performance on fluorescent membrane images (Ursell et al., 2017). Cellpose-SAM showed the best performance in benchmarking tests (mean F1 at IoU 0.8, 0.86±0.08), followed by Omnipose (0.76±0.16), Morphometrics (0.64±0.22), Cellpose3 (0.59±0.17) and microSAM (0.30±0.16) (Fig. 2a). Because segmentation algorithms are known to often fail on elongated cells, we further tested the performance of the fine-tuned models on a *Lysinibacillus* strains that naturally produces long cells under laboratory conditions (Supplementary Fig. 2b). Only Omnipose segmented long cells appropriately. The other models oversegmented them. Since our goal was to develop a pipeline for cell size analysis across different strains and species, many of which may naturally form long cells, we further analyzed Omnipose segmentation to improve its performance.

The fine-tuned Omnipose model produced segmentation masks lacking aberrations, truncations, and protrusions for isolated cells and individual cells within a chain, maintaining a proper rod-shaped morphology. However, it struggled with clustered cells, often producing indented or truncated masks (Supplementary Fig. 2a). We reasoned that this limitation might reflect the broader and less well-defined membrane signal in raw fluorescent images, particularly in densely packed regions (Hardo et al., 2024). To test whether improving membrane definition could enhance segmentation accuracy, we retrained Omnipose using deconvolved images. Deconvolution reduces out-of-focus blur and produces sharper membranes (Agard, 1984; Scalettar et al., 1996). When evaluated on deconvolved membrane images, the retrained model, FMSeg_Omni (hereafter

151 FMSeg), performed better than Omnipose retrained and evaluated on the corresponding raw
152 membrane images, and reached a performance better than that of Cellpose-SAM retrained and
153 evaluated on raw membrane images (mean F1 score at IoU 0.8, 0.88±0.09) (Fig. 2a). More broadly,
154 deconvolution affected model performance in a model-dependent manner (Fig. 2a; Supplementary
155 Fig. 2; Supplementary Fig. 3): Omnipose, microSAM and Morphometrics performed better on
156 deconvolved membrane images than on raw membrane images, whereas Cellpose-SAM and Cell-
157 pose3 showed the opposite trend, despite being fine-tuned separately for each image type.
158
159 FMSeg successfully identified and segmented single cells within groups, isolated cells, chains, and
160 even extremely elongated cells, regardless of the species or size (Fig. 2b,c; Supplementary Fig. 3).
161 Additionally, FMSeg successfully segmented yeast and cocci of various sizes, both isolated and
162 clustered, and worked with alternative membrane labels, including Mitotracker Green and GFP
163 fused to a homogeneously distributed membrane protein (QoxB) (Fig. 2d; Supplementary Fig. 4).

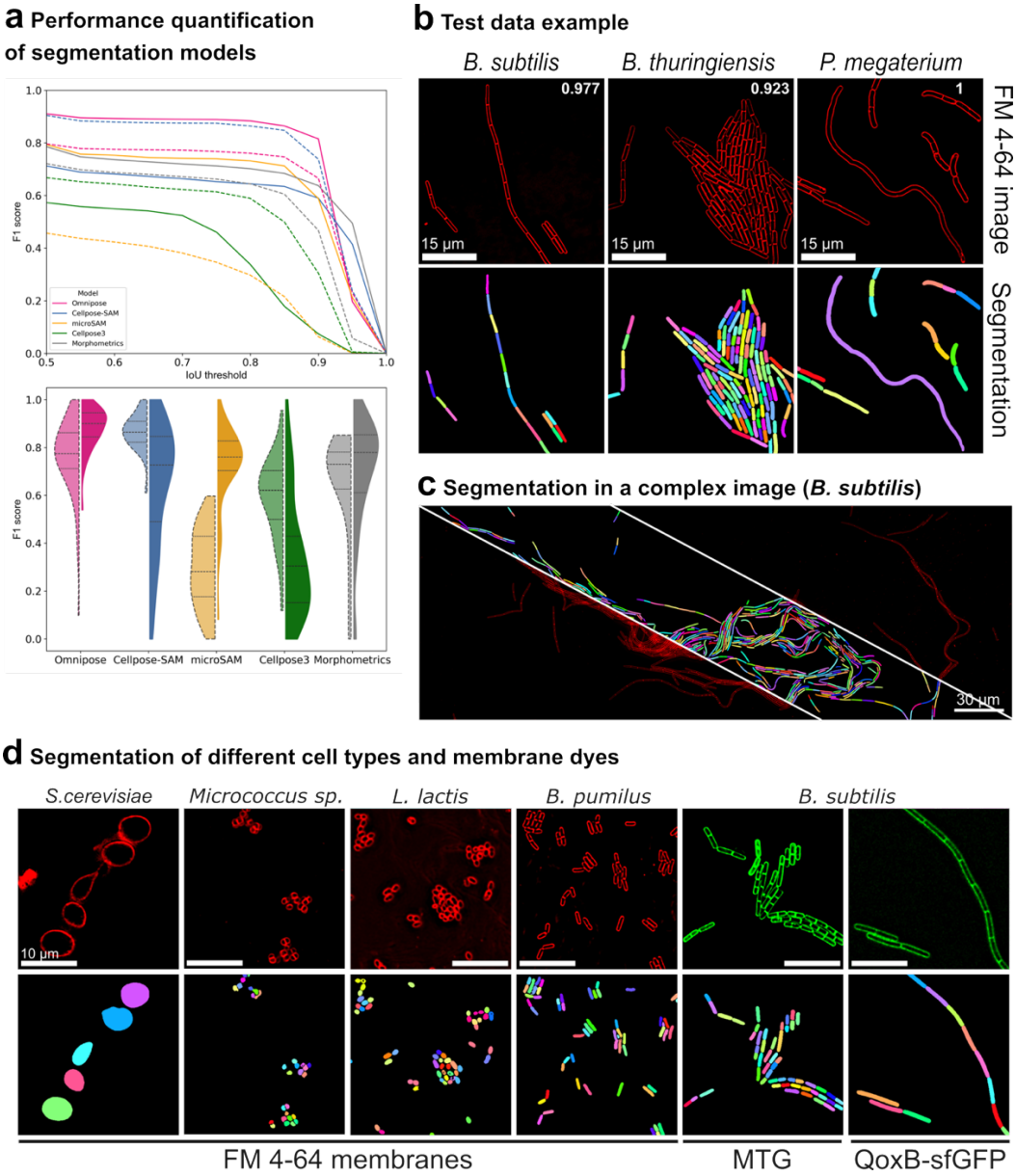

Figure 2. Evaluation of models for fluorescent-membrane segmentation. a, Quantitative benchmarking of Omnipose (pink), CellposeSAM (blue), microSAM (yellow), Cellpose3 (green) and Morphometrics (gray) on fifty-six images of *B. subtilis*, *B. thuringiensis* and *P. megaterium*. Omnipose, CellposeSAM, microSAM, and Cellpose3 were fine-tuned separately on raw and deconvolved fluorescent membrane images; models fine-tuned on raw images were evaluated on raw images, whereas models fine-tuned on deconvolved images were evaluated on deconvolved images. Top, F1 score across Intersection over Union (IoU) thresholds. Lines are the mean F1 scores of 56 images. Dashed lines correspond to model performance on raw fluorescent membrane images, and solid lines on deconvolved images. Bottom, F1 at IoU of 0.8. The first violin plot of each pair (lighter color and delineated by a dashed line) corresponds to model performance on raw images, and the second violin plot (darker color) to model performance on deconvolved images. The horizontal dashed line in the violin plots indicate the median, and the dotted lines the first and third quartiles. We called Omnipose model fine-tuned on deconvolved membranes FMSeg_omni (FMSeg) **b**, Examples of images showing chains, clusters, and heavily elongated cells. Top, deconvolved micrographs of *B. subtilis*, *B. thuringiensis* and *P. megaterium* cells stained with FM 4-64; bottom, FMSeg masks. F1 scores at IoU 0.8 are indicated at the top-right corner of each image. Scale bar, 15 µm. **c**, FMSeg segmentation of a *B. subtilis* microcolony. The image is split into three sectors. Segmentation results are shown in the middle sector, and FM 4-64 stained membranes in the flanking sectors. Scale bar, 30 µm. **d**, Segmentation of cells of different shapes and sizes, with membranes labeled with FM 4-64 or other fluorophores. Top, deconvolved fluorescent images; bottom, FMSeg segmentation. *Saccharomyces cerevisiae*, *Micrococcus sp.*, *Lactococcus lactis* and *B. pumilus* cells were stained with FM 4-64 (red). *B. subtilis* was stained with MitoTracker Green (MTG). We also imaged a *B. subtilis* strain producing a GFP fused to the membrane protein QoxB (QoxB-sfGFP, green), which is homogenously distributed in the membrane. See Supplementary Fig. 4 for benchmarking of MTG and QoxB-GFP segmentation. Scale bars, 10 µm.

To facilitate the segmentation of fluorescent membrane images acquired with different microscopes, including systems without deconvolution capabilities, we trained an image restoration model to predict deconvolution from non-deconvolved images (FM2FM model; Fig. 3a). When direct deconvolution of membrane images is possible, it can be used directly. FM2FM provides an alternative for datasets in which this is not feasible. FM2FM was trained using the CARE framework (Weigert et al., 2018), in which a supervised U-Net predicts pixelwise fluorescence values while accounting for spatial context (i.e. neighboring pixel intensities). The fluorescence profiles of the predicted images closely matched those of deconvolved images (Fig. 3a-c), and the model could generate images amenable for segmentation from different microscopes (Supplementary Fig. 5).

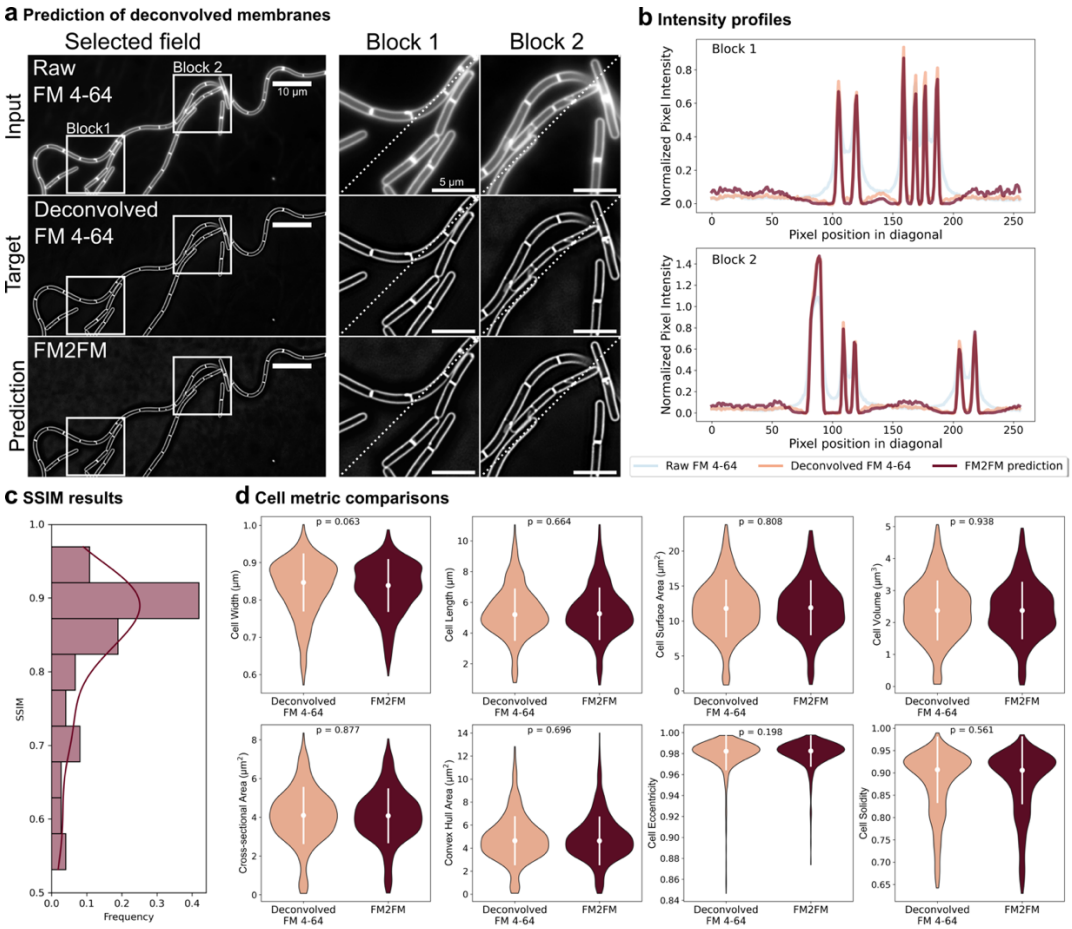

Figure 3. Deconvolution prediction. **a**, Example of deconvolution prediction with FM2FM. Top, input raw fluorescent membrane images (Raw FM 4-64); middle row, true deconvolved fluorescent membrane images (Deconvolved FM 4-64); bottom, FM2FM-predicted image. White squares mark regions zoomed in at right (Block 1 and Block 2). Diagonal dotted lines indicate profile traces in **b**. Scale bars: full images, 10 µm; zoomed-in blocks, 5 µm. **b**, Fluorescence profiles across the dotted lines in Block 1 (top) and Block 2 (bottom). Light blue, raw FM 4-64; orange, deconvolved FM 4-64; burgundy, FM2FM prediction. **c**, Structural similarity index measure (SSIM) between FM2FM predicted images and deconvolved images. The distribution of SSIM values across 74 image crops is shown. **d**, Violin plots of cell width, length, surface area, volume, cross-sectional area, convex hull area, eccentricity and solidity calculated from deconvolved FM 4-64 images (orange) and FM2FM-predicted images (burgundy). The white dots and vertical lines within the violin plots represent the medians and standard deviations. P values from statistical comparisons between distributions (ANOVA or Kruskal test; see methods for details) are indicated in each panel. Twenty images (over 1000 cells) were processed and segmented with FMSeg. See the Methods for size calculation details.

To assess whether deconvolution prediction affects segmentation, we compared cell size parameters—width, length, cross-sectional area, surface area and volume (see next section and methods for details)—extracted from masks generated using deconvolved and FM2FM-predicted images. We used multiple size metrics to verify that information relevant to downstream analyses is preserved across processing scenarios, as single metrics often fail to predict how image-derived measurements propagate into downstream results (Gunawan et al., 2025). We also compared shape descriptors not directly related to cell size, such as convex hull area, eccentricity and solidity. The distributions were very similar, with no statistically significant differences (Fig. 3d), indicating that membrane deconvolution prediction from raw membrane images has a minimal effect on segmentation and does not impact cell size calculations.

Additionally, we trained a fluorescence translation model to infer deconvolved membranes from cytoplasmic fluorescence (FP2FM model; Supplementary Fig. 6), which might be useful when membrane staining is not feasible. Previously developed CARE restoration models for the prediction of superresolution membranes can also be used (Spahn et al., 2022). Although these approaches expand the applicability of the method, they may introduce biases on cell size measurements (Supplementary Fig. 6).

Altogether, our fine-tuned segmentation and deconvolution prediction models offer a robust approach for the high-throughput segmentation of individual bacterial cells with fluorescent membranes, regardless of their size, shape and chaining pattern.

MEDUSSA, an analytical pipeline for extracting cell size from fluorescent membrane images.

We designed an algorithm to extract precise 2D cell dimensions—width and length—and extrapolate 3D measurements such as membrane surface area and volume (Fig. 4a). Starting from FMSeg-generated masks, we applied a distance transform to compute, for each pixel, the shortest distance to the mask periphery. We then overlaid a medial skeleton on this transform and sampled the radius along the skeleton to obtain cell width across the long axis. Radii at the skeleton endpoints were used to estimate the size of the hemispherical caps, yielding length and width profiles for each cell. Assuming rotational symmetry and imaging in the medial focal plane, we estimated volume and surface area by summing cylindrical segments along the skeleton and adding hemispherical ends. Additional details are provided in the Methods section.

Integrating segmentation with size calculations revealed two key factors critical for reliable measurements (Fig. 4b-d; Supplementary Fig. 7; Supplementary Fig. 8). The first is that the size of the segmentation masks is sensitive to the focal plane (Fig. 4b,c; Supplementary Fig. 7). For rod-shaped cells, width is maximal at the mid-cell focal plane but decreases above and below it (Fig. 4c) (Ursell et al., 2017). It is therefore critical to ensure that size measurements are taken from mid-cell focal planes. However, due to minor aberrations in microscopy slides, cells within a field of view often reside in slightly different focal planes (Fig. 4b; Supplementary Fig. 7). To address this, we acquired z-stacks and projected them onto a single plane before predicting deconvolution with FM2FM and segmentation (Fig. 4b). This approach yielded size estimations equivalent to those obtained from mid-cell focal planes (Fig. 4c), enabling accurate measurements across entire microscopy field, regardless of focal plane differences.

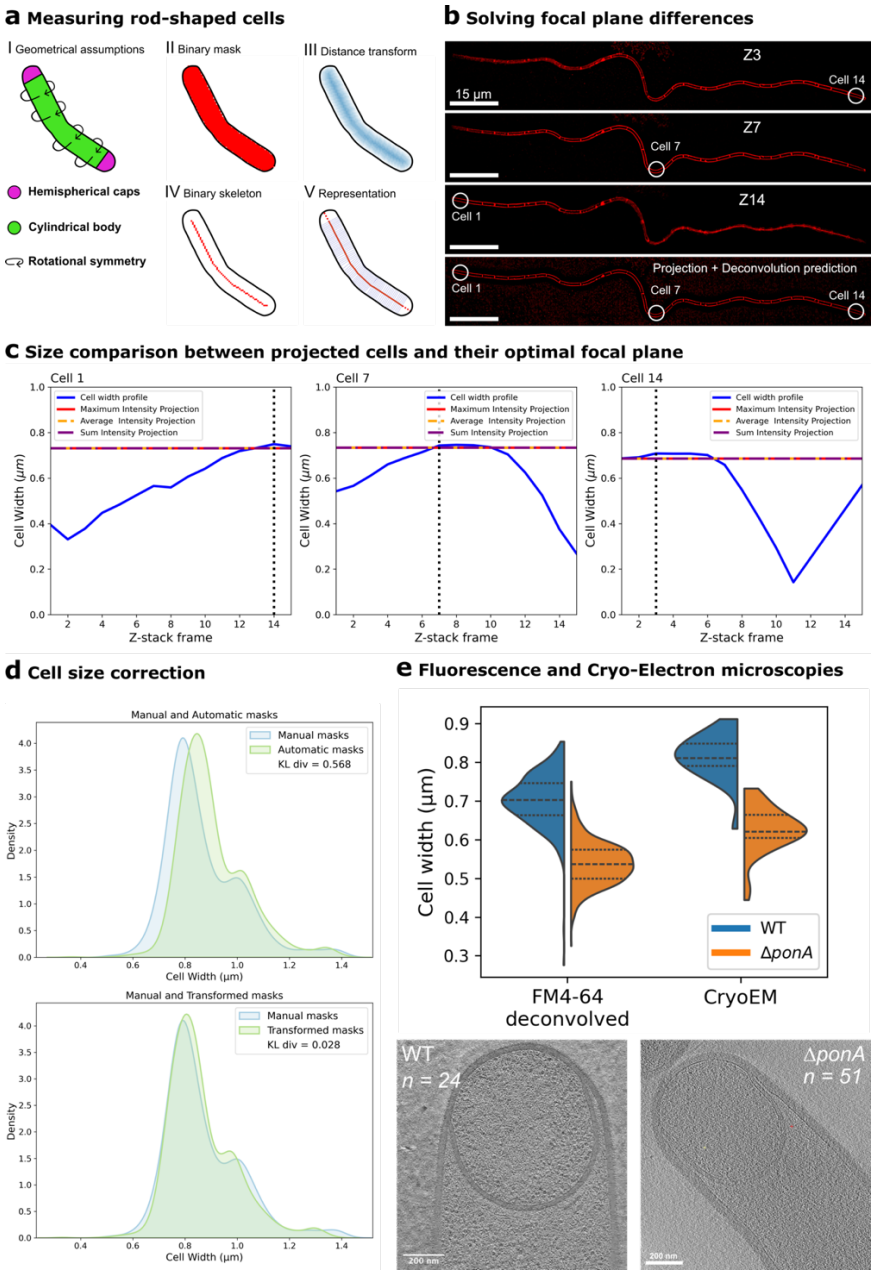

Figure 4. Cell size estimation from fluorescent-membrane segmentation masks. a, Cell size calculation workflow. **b**, Representative z-slices from an optical-sectioning stack of a 14-cell *B. subtilis* chain stained with FM 4-64. Different cells are in focus in different slices. Circled cells are analyzed in **c**. The last image is a maximum-intensity projection of whole stack, processed FM2FM, where all cells appear in focus. Scale bar, 15 μm. Full stack in Supplementary Fig. 3. **c**, Width profiles (solid blue lines) of the cells circled in **b** on different z-slices across the optical sectioning stack: Cell 1 (right graph), Cell 7 (middle graph) and Cell 14 (right graph). Width is maximized on the slice in which the cell is in focus (vertical dotted lines). Cell width calculated from projected images is indicated by horizontal dashed lines. Results were equivalent regardless of the projection type (maximun intensity, red dashed line; average intensity, orange dashed line; sum, purple dashed line). Cells were segmented using JFilament in every z-slice and projections with FMSeg. **d**, FMSeg masks are slightly wider than manual JFilament masks. Density plots show the width distribution of 1100 bacilli cells. The top plot compares JFilament masks (blue) to FMSeg masks (green). After transforming the data with our sampling strategy (transformed masks, bottom plot), the distributions align better. The similarity of the distributions was quantitatively compared using Kullback–Leibler Divergence (KL div, values in insets within the graphs). See Supplementary Fig. 8 and the Methods section for details. **e**, Widths of wild-type (WT, blue) and Δ*ponA* (orange) cells from sporulating *B. subtilis* cultures, measured from deconvolved fluorescent-membrane images segmented with FMSeg (FM 4-64 deconvolved; 326 and 617 cells for WT and Δ*ponA*, respectively), or from CryoEM images (24 and 51 cells for WT and Δ*ponA*, respectively). Dashed lines mark the median: WT 0.70 μm (FM) vs 0.81 μm (cryo-EM); Δ*ponA* 0.54 μm (FM) vs 0.63 μm (cryo-EM). FM widths were ~14% lower than cryo-EM, but the WT/ΔponA ratio was nearly identical (1.300 vs 1.304; <1% difference). Cryo-EM images courtesy of E. Tocheva (Δ*ponA*) and E. Villa & K. Khanna (WT).

Second, we observed that the FMSeg model consistently generated masks slightly wider than ground truth masks (Fig. 4d; Supplementary Fig. 8a). This bias propagated into surface area and volume calculations (Supplementary Fig. 8b). Fortunately, the overestimation was independent of cell size, allowing us to apply a systematic correction (Fig. 4d; Supplementary Fig. 8b). We developed a size correction pipeline that allowed us to predict the "true" cell size based on the dimensions of FMSeg-generated masks (Supplementary Fig. 8; see methods for details). We validated this approach by correcting the segmentation outputs for *B. subtilis*, *B. thuringiensis* and *P. megaterium* cells used in our benchmarking tests (Fig. 2a). As shown in Fig. 4d, FMSeg-mask width distribution was slightly shifted compared to that obtained from ground-truth masks generated using JFilament. After applying the correction, both distributions became nearly identical (Fig. 4d).

To assess the accuracy of our cell size measurements, we compared estimates from our pipeline with those obtained from plunged-frozen *B. subtilis* imaged by cryo-electron microscopy (cryoEM), a technique that provides high-resolution images of cells preserved in their native physiological state. We focused on sporulating *B. subtilis* cells, as we could access sets of cryoEM images of these cells, kindly provided by Elitza Tocheva (Tocheva et al., 2013), and Elizabeth Villa and Kanika Khanna (Khanna et al., 2021; Khanna et al., 2019; Lopez-Garrido et al., 2018). To test robustness across different cell sizes, we measured both wild type cells and cells lacking PBP1 (Δ*ponA*), which are ~25% thinner than wild type cells (Popham & Setlow, 1996). Our pipeline reproduced the difference in width between wild-type and Δ*ponA* cells observed by cryo-EM, although the absolute width estimates were on average ~14% lower than those obtained by cryo-EM (Fig. 4e). This discrepancy may reflect a systematic bias in our fluorescence-based measurements, but it could

298 also arise from differences in sample preparation, imaging modality, or growth conditions between
299 the two datasets. These results indicate that our pipeline provides realistic cell size estimates and
300 is robust to biologically relevant differences in cell width.
301
302 Overall, our fine-tuned segmentation model, coupled with deconvolution prediction and size cor-
303 rection, enables high-throughput, reliable cell size measurements from fluorescent-membrane mi-
304 croscopy images. We refer to the full pipeline for bacterial cell-size measurement as MEDUSSA
305 (MEmbrane DeconvolUtion and Segmentation for Size Analyses) (Supplementary Fig. 9).
306
307 **Insight into intraspecific cell-size diversity in *P. megaterium*.**
308 We applied MEDUSSA to study variation in cell size across strains of *P. megaterium* (de Bary, 1884),
309 a member of the *Bacillaceae* generally considered to produce large cells but for which intraspecific
310 morphological diversity has been reported (Logan & Vos, 2015; López & Alippi, 2009; Murumkar
311 et al., 2012). We focused on six strains widely used in physiology and biotechnology: the type strain
312 DSM 32 (ATCC 14581) (Arya et al., 2014) from the German Collection of Microorganisms and
313 Cell Cultures (DSMZ); the classic multi-plasmid strain QM B1551 (Eppinger et al., 2011); the
314 naturally plasmidless strain DSM 319 (Eppinger et al., 2011; Stahl & Esser, 1983); KM, used in
315 early bacteriophage studies; 899, also used in early bacteriophage and bacteriocin studies; and
316 WH320 (Rygus et al., 1991), a Lac^- derivative of DSM 319 commercially available for protein-
317 expression. We sampled cultures of each strain during exponential and stationary phases in LB
318 medium (Supplementary Fig. 10), imaged them in agarose pads supplemented with FM 4-64 for
319 membrane staining, and processed the images through our complete pipeline to obtain estimations
320 of the sizes of individual cells (Fig. 5; Supplementary Fig. 11a). Although all strains tended to form
321 chains (Fig. 5a), MEDUSSA could resolve single cells with high precision. Single-cell dimensions
322 were generally consistent across experimental runs, although we observed variation in population
323 averages of some strains (up to 27% for cell length and 12% for cell width; Supplementary Fig.
324 11a) likely due to day-to-day differences in conditions outside experimental control. Technical
325 variation among samples from the same culture was low (2-3% at most for cell width and length)
326 (Supplementary Fig. 11b).
327
328 We observed striking between-strain diversity in cell width: during exponential growth, median
329 width ranged from 0.92 μm in WH320 to 1.39 μm in 899 (Fig. 5b; Supplementary Figure 11a).
330 Most strains were slightly thinner in stationary phase, except KM, whose width distribution broad-
331 ened without a clear shift in the median (Fig. 5b). Although width showed a smaller coefficient of

variation (CV) than length—consistent with tighter control—the width CVs of *P. megaterium* strains were generally higher than those reported for *B. subtilis* (Juillot et al., 2021; Nordholt et al., 2020; Sauls et al., 2019; Taheri-Araghi et al., 2015; also reproduced by us in Supplementary Fig. 11a), with some strains reaching ~0.15 in exponential or stationary phase (Supplementary Fig. 11a). Notably, cells of different widths were sometimes present within a single chain (arrowheads in Fig. 5a).

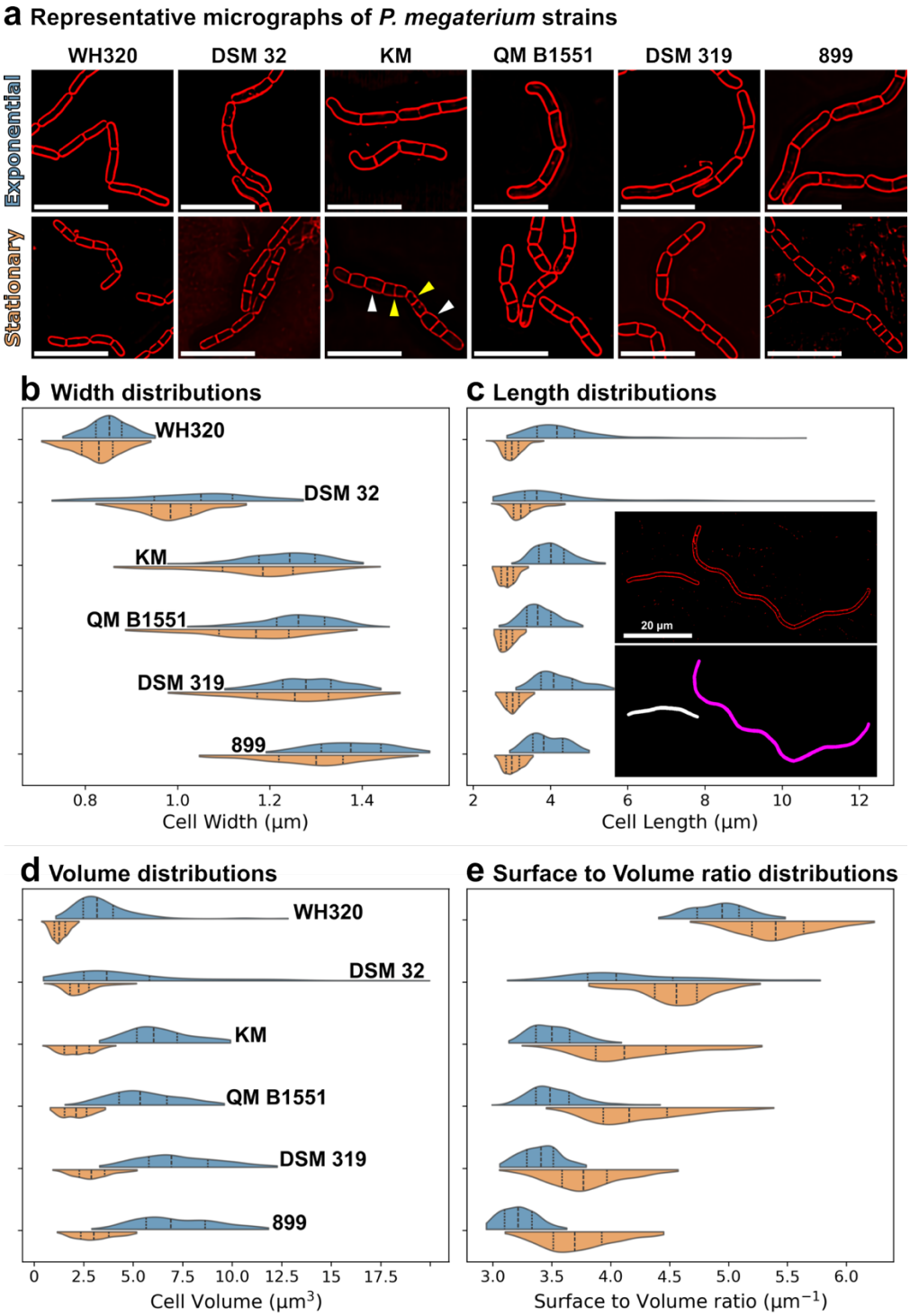

Figure 5. Morphological characterization of six *P. megaterium* strains. a, Fluorescence micrographs of FM 4-64-stained cells of different *P. megaterium* strains sampled form exponential and stationary phase LB cultures: WH320, DSM 32, KM, QM B1551, DSM 319 and 899. Arrowheads in the KM stationary image point to thicker (white) and thinner (yellow) cells within a chain. Scale bars, 10 μm. **b-e,** Distributions of cell with (**b**), length (**c**), volume (**d**) and surface to volume (**e**) for the indicated strains (strain names in panel **b** and **d**; same order maintained in the other panels) during exponential (blue) and stationary (orange) phase. The dashed line in the violin plots indicate the median, and the dotted lines the first and third quartiles. The inset in panel **c** shows a micrograph of a long cell produced by DSM 32 during exponential growth (membranes, red; scale bar, 20 μm). The following number of cells were analyzed for each strain in exponential and stationary phase: WH320, 153 and 961 cells; DSM 32, 192 and 904 cells; KM, 149 and 856 cells; QM B1551, 292 and 447 cells; DSM 319, 195 and 471 cells; 899, 758 and 548 cells. The central 95% of observed values are represented. See Supplementary Fig. 11 for comparison between experimental runs. Prior to measurement, segmentation output was manually curated to remove aberrant masks and truncated masks at image edges.

We also observed significant differences in cell length across strains: in exponential phase, the median ranged from 4.06 μm in DSM 32 to 5.76 μm in strain 899, and cells shortened in stationary phase, as expected (Fig. 5a,c). Within-strain variation in cell length was high in some cases (Figure 5c; Supplementary Fig. 11a), with rare, extremely elongated cells occurring in several strains; the more dramatic cases were in DSM 32, where approximately 10% of the cells were over 10 μm long (Fig. 5c, inset). These extreme elongation events were not observed in stationary phase (Figure 5c), suggesting that it is a phenomenon associated with active growth and that these filaments septate into multiple cells or lyse upon entry into stationary phase.

These width and length differences underpinned differences in surface-to-volume ratios—thinner cells exhibited higher surface-to-volume ratios than thicker cells (Ojkic et al., 2019, 2022)—and contributed to the diversity of cell volumes observed between strains, spanning nearly threefold (Fig. 5d-e).

P. megaterium WH320 carries a partially functional version of PBP1.

Most accounts of *P. megaterium* cell width report values of ~1.2-1.5 μm (Logan & Vos, 2015). However, two of our strains, DSM 32 and WH320, had widths below these values. We were particularly surprised by WH320, whose median width during exponential growth was ~0.9 μm, as this strain is a derivative of DSM 319, one of the thickest strains in our panel (median width in exponential phase ~1.4 μm).

WH320 was generated by ethyl-metanosulfonate (EMS) mutagenesis of DSM 319, selecting for Lac⁻ clones (Rygus et al., 1991). One potential explanation for the reduced cell width of WH320 is that an additional mutation introduced during EMS mutagenesis or at some point after the two strains diverged affected cell width. To explore this possibility, we sequenced the genome of WH320 and compared it to the parental DSM 319 reference genome (Eppinger et al., 2011). The

379 two strains differed by 37 single nucleotide polymorphisms, with the majority of them being
380 G·C→A·T transitions, consistent with EMS mutagenesis (Sega, 1984) (Supplementary Data in
381 Zenodo repository). We also observed other mutations including transversions and indels, which
382 might have occurred during transfer of the strains in the lab before we acquired them. One of the
383 transitions caused a glycine-to-arginine amino acid substitution in the catalytic site of *P. megaterium*
384 β-galactosidase, likely responsible for the Lac⁻ phenotype. We also found a C to A transversion in
385 *ponA* that produced an alanine-to-aspartic acid change at residue 214 in the transglycosylase do-
386 main of the classA penicillin binding protein PBP1 (Supplementary Data in Zenodo repository).
387

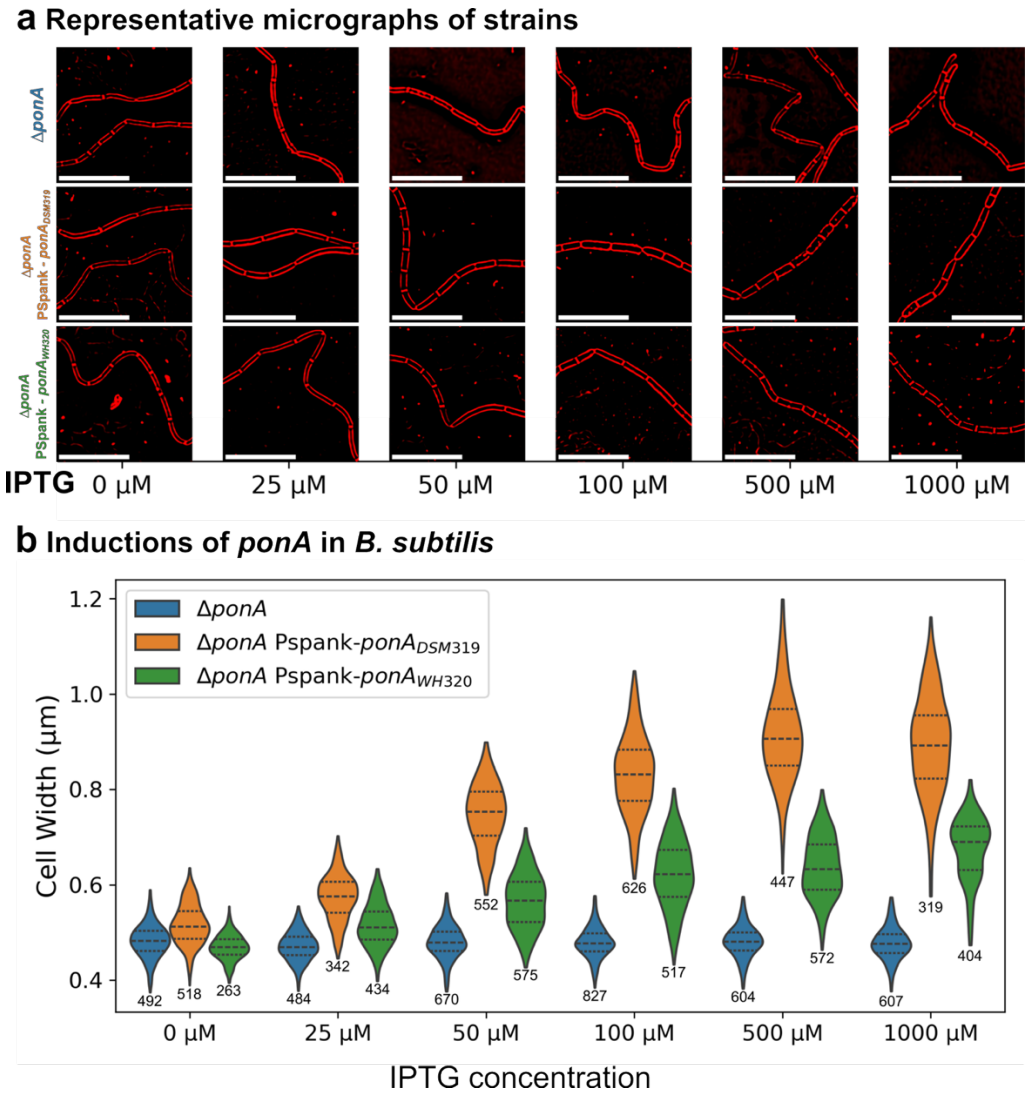

388

389 **Figure 6. WH320 carries a hypomorphic PBP1 allele**. **a,** Representative FM 4-64-stained cells corresponding to
390 panel b. Scale bar, 10 μm. **b,** Cell width of a *B. subtilis* PY79 *ponA* mutant (Δ*ponA*, blue) and the same mutant expressing
391 *P. megaterium* DSM 319 *ponA* (Δ*ponA* P_{spank}-*ponA*$_{DSM319}$, orange) or *P. megaterium* WH320 *ponA* (Δ*ponA* P_{spank}-*ponA*$_{WH320}$,
392 green) from the IPTG-inducible P_{spank} promoter inserted at the *amyE* locus. Violin plots show width distributions at
393 different IPTG concentrations. Central 99% of data points was sampled for each strain in each condition. The dashed
394 line indicates the median; dotted lines mark the first and third quartiles. The number of cells for each violin is shown
395 in the plot under each violin. Prior to measurement, segmentation output was manually curated to remove aberrant
396 masks and truncated masks at image edges. Width distributions of the three strains were statistically different from
397 each other at all IPTG concentrations (Kruskal test).

398

399 As noted above, PBP1 modulates cell width in *B. subtilis*, with *ponA* mutants being ~25% thinner
400 that the wild type and *ponA* overexpression producing cells thicker than the wild type (Fig. 4e)
401 (Dion et al., 2019; Popham & Setlow, 1996). We therefore hypothesized that the *ponA* mutation
402 reduces PBP1 activity and underlies the thin phenotype of WH320. To get insight into this possi-
403 bility, we asked whether the *ponA* alleles from DSM 319 and WH320 could complement a *B. subtilis*
404 *ponA* mutant when produced ectopically. We placed both alleles under the IPTG-inducible pro-
405 moter P_{spank} at the ectopic *amyE* locus, and measured cell width after incubation with varying IPTG
406 concentrations. As shown in Fig. 6, expression of DSM319 *ponA* produced a marked increase in
407 cell width, even at low IPTG concentrations. In contrast, expression of WH320 *ponA* caused a
408 milder increase in cell width and never reached the values observed with $ponA_{DSM319}$, even at high
409 induction levels. These results indicate that the alanine-to-aspartate substitution in *ponA* reduces
410 PBP1 function.

411 **DISCUSSION**
412

413 Here, we introduce MEDUSSA, an image-analysis pipeline that extracts accurate single-cell size
414 measurements from fluorescent-membrane microscopy images, and demonstrate its utility for dis-
415 secting mechanisms of cell-size diversity among bacterial strains. The workflow combines deep-
416 learning–based image restoration for deconvolution prediction with automated segmentation to
417 delineate cell boundaries from membrane signal, followed by mask analysis to estimate cell size.
418 Because each step is modular, the restoration (FM2FM), segmentation (FMseg), and measurement
419 components can be used independently to suit specific study needs (Supplementary Fig. 9). Ap-
420 plied across strains and species, MEDUSSA yields cell-size measurements that can be further in-
421 terrogated to identify underlying mechanisms.
422

423 MEDUSSA is well suited for comparative studies because it addresses key shortcomings of previ-
424 ous methods. First, fluorescent membrane imaging enables precise delineation of cell boundaries
425 by tracking the peak membrane signal around each cell (Fig. 1). This supports consistent training-
426 set annotation and yields more reliable cell-size estimates than phase-contrast-based approaches
427 (Hardo et al., 2024) (Fig. 1). Second, membrane dyes reveal septal membranes, allowing clear sep-
428 aration of daughter cells that remain attached after division and thus enabling reliable length meas-
429 urements for both isolated cells and chains—something that is difficult with phase contrast (Fig.
430 1) (Syvertsson et al., 2016). Third, the pipeline corrects focal-plane differences among cells within
431 the same image, which would otherwise bias measurements because focal-plane shifts alter mask
432 size (Fig. 4b-c) (Ursell et al., 2017). Specifically, projecting fluorescence images from a z-stack and
433 applying a deconvolution-prediction restoration algorithm (FM2FM) produces segmentation-
434 ready images that yield mid-focal-plane masks. Thus, this standardized protocol of restoration,
435 segmentation, and measurement converts membrane-fluorescence images into population-level
436 size distributions.
437

438 A trade-off is the need for fluorescent labeling. Several membrane and cell-wall dyes are routinely
439 used in bacterial cell biology (Greenspan & Fowler, 1985; Herman et al., 1994; Kuru et al., 2012;
440 Lucidi et al., 2024; Monteiro et al., 2015; Pogliano et al., 1999; Sharp & Pogliano, 1999). Most
441 experiments presented here use FM 4-64, a lipophilic styryl fluorophore that associates with the
442 outer leaflet of the cytoplasmic membrane without disrupting membrane function (Pogliano et al.,
443 1999). FM 4-64 is broadly applicable across bacterial species and compatible with live-cell imaging
444 (Calvez et al., 2019; Dalebroux et al., 2015; Ma et al., 2009; Maloney et al., 2009; O'Hara et al.,
445 2017; Ojkic et al., 2016; Shin et al., 2015; Specht et al., 2013; Studer et al., 2016; Sun & Margolin,

446 1998; Tsuge et al., 2008; Yeh et al., 2010). However, our segmentation model also works with
447 other labels—including the membrane-permeable MitoTracker Green and with GFP fused to a
448 membrane protein (Fig. 2d; Supplementary Fig. 4)—and, in principle, with any dye that provides
449 uniform signal along the cell periphery. In addition, we provide a transformation model, FP2FM,
450 that predicts membrane-like boundaries suitable for segmentation from cytoplasmic fluorescence,
451 adding flexibility (Supplementary Fig. 6). Altogether, the available dyes, combined with the trans-
452 formation tools provided here and elsewhere (Spahn et al., 2022), extend the applicability of the
453 MEDUSSA method to a broad range of species. For direct comparisons, we recommend using
454 the same staining modality and image transformation procedures, because different labels or trans-
455 formation models may slightly affect size estimations. For example, FM 4-64 labels the outer leaflet
456 of the cytoplasmic membrane, whereas GFP fused to a membrane protein is displaced toward the
457 cytoplasmic side. Consequently, boundaries inferred from GFP-based signals may appear slightly
458 inward relative to those inferred from FM 4-64, leading to systematic differences in estimated cell
459 size (Supplementary Fig. 12).
460
461 Although MEDUSSA addresses several limitations associated with cell-size estimation from
462 phase-contrast images, it does not overcome challenges inherent to the imaging of small bacterial
463 cells by optical microscopy. A single pixel in a fluorescence microscopy image may amount to 10%
464 of the width of a typical bacterial cell, so even minor segmentation imprecisions can translate into
465 appreciable differences in measured size. For reliable comparisons between strains and replicates,
466 it is therefore important to quantify sufficiently large numbers of cells, and compare the size dis-
467 tributions of the populations. Bacterial cell size also depends on growth conditions (Schaechter
468 et al., 1958), and biological variation between cultures can be substantial depending on media and
469 growth stage (Bakshi et al., 2021; Cylke & Banerjee, 2023; Kellogg & Levin, 2022). We therefore
470 recommend to keep growth conditions as constant as possible to obtain biologically meaningful
471 and reproducible results.
472
473 Segmentation accuracy also depends on image quality. In particular, images with low signal-to-
474 noise ratios can result in lower segmentation accuracy (Supplementary Fig. 13). To mitigate this
475 limitation, we trained an additional CARE restoration model (FM2FM-HiSNR; see methods for
476 details) that predicts high signal-to-noise deconvolved membranes across a range of input signal-
477 to-noise levels. Under our imaging conditions, restoration with this model improves the segmen-
478 tation quality of low signal-to-noise images (Supplementary Fig. 13), although extremely low signal
479 levels will ultimately limit segmentation accuracy.

480

481 In addition, projection artifacts can lead to cell-size misestimation from fluorescent images, an
482 effect that may be particularly pronounced for smaller cells (Hardo et al., 2024; Ursell et al., 2017).
483 Hardo et al. reported marker-dependent biases, with membrane fluorescence tending to underes-
484 timate cell width and cytoplasmic fluorescence tending to overestimate it, and with proportionally
485 larger effects in thinner cells (below ~1 μm) than in thicker cells. To probe for this effect under
486 our imaging and analysis conditions, we compared cell width estimates derived from independently
487 segmented membrane and cytoplasmic fluorescence across a controlled width range (*ponA* under
488 IPTG; Supplementary Fig. 14). If projection artifacts were prominent under our conditions, we
489 would expect cytoplasmic-fluorescence-based estimates to be relatively larger than membrane-
490 based estimates for thin cells, with the discrepancy decreasing as cells become thicker. However,
491 width scaled almost identically when estimated from membrane and cytoplasmic fluorescence
492 across the tested width range (~0.6-1.2 μm) (Supplementary Fig. 14b). These results suggest that
493 projection artifacts, as described by Hardo et al., do not measurably bias our width estimates under
494 these conditions, although they may become more relevant in cells thinner than those examined
495 here or under different imaging settings.

496 In this study, we applied MEDUSSA to quantify the size of six strains of *P. megaterium*. Our
497 measurements reveal remarkable diversity in cell size both among strains and among individual
498 cells within a strain (Fig. 5). Although all strains produce comparatively large cells by bacterial
499 standards, some produce cells that are, on average, over twofold larger in volume than others. We
500 also observed that some strains formed extremely elongated cells during exponential growth,
501 which were not observed in stationary phase. To our knowledge, filamentation has not been
502 reported previously in *P. megaterium*—likely because membrane dyes are not routinely used in
503 microscopy. The mechanism underlying this filamentation, and whether such filaments occur in
504 nature or are artifacts of laboratory culture, remains to be determined.

505 Cell width in bacteria is generally assumed to be tightly controlled within a species, with little cell-
506 to-cell variation in steady state cultures (Campos et al., 2014; Chien et al., 2012; Ojkic & Banerjee,
507 2021; Ojkic et al., 2022; Sauls et al., 2019; Taheri-Araghi et al., 2015). Our dataset, however, reveals
508 substantial width variation both within and between strains. Within strains, width values were
509 approximately normally distributed, and some strains showed wide cell-to-cell variation; for
510 example, in strain KM during stationary phase, the thinnest cells were up to twofold thinner than
511 the thickest cells (Fig. 5). The coefficient of variation for width reached up to 0.15 (Supplementary

512 Fig. 11)—more than twice that of *B. subtilis*—suggesting that mechanisms of width homeostasis
513 in this bacterium are less precise than in *B. subtilis* (Nordholt et al., 2020; Sauls et al., 2019).

514 Between strains, width distributions were shifted, with median widths ranging from ~0.9 to 1.4
515 μm (Fig. 5; Supplementary Fig. 11a), indicating variation in width regulation across strains. We
516 further examined differences between the thick strain DSM 319 and its Lac⁻ derivative WH320,
517 which is ~0.5 μm thinner. Genome comparison revealed an alanine-to-aspartic acid substitution
518 in the transglycosylase domain of PBP1. An alignment of PBP1 sequences from 854 strains
519 indicates that alanine at position 214 is largely conserved (~75%); ~24% carry serine at this
520 position, and fewer than 1% contain other residues (e.g., cysteine, threonine, valine)
521 (Supplementary Data in Zenodo repository). Notably, no sequence harbors an aspartic acid or any
522 other charged residue at this position, suggesting that introducing charge there impairs PBP1
523 activity. Because PBP1 mutants yield thinner cells in *B. subtilis* (Popham & Setlow, 1996), it is
524 plausible that the hypomorphic PBP1 allele in *P. megaterium* WH320 contributes—at least in part—
525 to its reduced width relative to the DSM 319 parental strain.

526 Unlike the mutation in *lacZ*, the *ponA* mutation in *P. megaterium* WH320 is a G→T transversion.
527 Because EMS typically induces G·C→A·T transitions (Sega, 1984), it is unlikely that the *ponA*
528 mutation arose directly from EMS mutagenesis. Instead, we suspect that the *ponA* mutation in
529 strain WH320 was either already present in the DSM 319 clone used for EMS treatment or was
530 acquired during subsequent propagation of WH320 before we received the strain.

531 Overall, these results illustrate how MEDUSSA can be used to explore within- and between-strain
532 diversity in bacterial cell size and to reveal differences that can be pursued to identify underlying
533 mechanisms. Future work will expand our strain set and survey additional species and
534 environmental isolates to advance our understanding of the evolution of bacterial cell size and
535 contribute to the emerging field of evolutionary cell biology (Jiang et al., 2015; Lynch et al., 2014).

536 **METHODS**

537

538 **Strains and plasmids**

539 A list of strains is provided in Supplementary Table 1. Plasmid and primer lists are in Supplemen-
540 tary Tables 2 and 3, along with detailed descriptions of plasmid construction.

541

542 **Culture media and growth conditions**

543 Bacteria were routinely grown on LB agar plates (Lennox formulation, 5 g NaCl/L) overnight at
544 30 °C, with the exception of *Lactococcus lactis*, which was grown on MRS medium at 28 °C. *Saccha-*
545 *romyces cerevisiae* was grown on YPD at 37°C.

546 For size quantification of *B. subtilis* and *P. megaterium* strains, a single colony was inoculated into 5
547 mL fresh LB Lennox and grown overnight in a roller drum at 30 °C with constant rotation. The
548 next morning, cultures were diluted 1:1000 into 30 mL of the appropriate medium in 250-mL
549 baffled flasks and incubated in a water bath at 30 °C with shaking at 220 rpm. Samples were taken
550 after five hours (exponential; Supplementary Fig. 10) and after ten hours (stationary;
551 Supplementary Fig. 10) for microscopy (see next section).

552 For the induction experiments shown in Fig. 6 and Supplementary Fig. 14, a single colony was
553 inoculated into LB Lennox diluted 1/4, then grown at 25 °C in a shaking incubator at 220 rpm.
554 The next morning, cultures were diluted to an OD600 of 0.02 in 1/4-diluted LB Lennox with the
555 indicated IPTG concentration (0, 25, 50, 100, 500, or 1000 μM). Cultures were grown at 30 °C in
556 a shaking incubator to an OD600 of 0.2–0.5 and then samples were taken for microscopy.

557 Sporulation (Fig. 4e) was induced by resuspension, as described elsewhere (Riley et al., 2018).

558 **Microscopy**

559 For imaging, 10 μL culture samples were imaged on 1.2% agarose pads in 1/4-diluted LB-Lennox
560 supplemented with 0.5 μg/mL FM4-64. The pad was covered with a #1.5 glass coverslip. Ten-
561 hour samples were diluted tree times to avoid overcrowded fields.

562

563 For cell-size estimation experiments for the different *B. subtilis* and *P. megaterium* strains, cells were
564 imaged using a Leica Thunder Imager live cell with a Leica DFC9000 GTC sCMOS camera and a
565 100X HC PL APO objective (Numerical aperture 1.4, Refractive index 1.518 objective). FM 4-64
566 images were taken using a 510 nm excitation LED light source, with 70% intensity and 0.1 s
567 exposure, and a custom filter cube produced by Chroma Technology GmbH (Olching, Germany)

568 with the following components: excitation filter, ET505/20x; dichroic mirror, T660lpxr; emission
569 filter, ET700lp. Training images for the restoration (FM2FM and FM2FM-HiSNR) and translation
570 (FP2FM) models were taken with a DeltaVision Ultra microscope with a PCO Edge sCMOS
571 camera and an Olympus 100X UPLX APO objective (Numerical aperture 1.45, Refractive index
572 1.518 Ph3). FM 4-64 and mVenusQ69M were visualized with the following filters: excitation 542
573 nm and emission 679 nm for FM 4-64, and excitation 475 nm and emission 525 nm for
574 mVenusQ69M, with light transmission at 100% and an exposure time of 0.2 s for both channels.
575 Training images for the segmentation models (FMSeg, RawFMSeg) were taken using the same
576 illumination conditions as the restoration model. For the membrane images of *E. coli*, the FM4-64
577 was captured with light transmission of 40% and an exposure time of 0.1 s.

578 For phase-contrast microscopy, the aforementioned DeltaVision microscope was used, light
579 transmission was set to 100% and exposure time to 0.1 s.

580 For microscopy comparisons, we also used a Zeiss Axio Imager Z2 microscope with a Hamamatsu
581 sCMOS camera and a Zeiss 100x Plan-Apochromat objective (Numerical aperture 1.40, Refractive
582 index 1.518 Ph3). FM 4-64 was visualized with an excitation filter of 506 nm and emission filter
583 of 751 nm, with light transmission at 100% and an exposure time of 0.2 s.

584 **Ground truth image annotation using active contours**

585 We annotated cells in our ground-truth images using the ImageJ plugin JFilament (Smith et al.,
586 2010), which allows the semi-automatic generation of sub-pixel resolution active contours (snakes)
587 that follow the ridges of maximum fluorescence membrane intensity around the cell (Fig. 1f; Sup-
588 plementary Fig. 1) (Lopez-Garrido et al., 2018; Ojkic et al., 2014, 2016). Default parameters were
589 used except for Gamma, which we increased when the preset value caused excessive deformation
590 of the snakes. For cell clusters, snakes were typically manually corrected because contour edges
591 tended to deform toward neighboring cells. When membrane blobs distorted cell contours, we
592 also corrected the snakes to follow an appropriate straight line. These steps ensured consistent
593 single-cell segmentation for model training and improved robustness of the segmentation model
594 to such confounding artifacts.
595

596 **Training and evaluation of models for segmenting fluorescent membranes.**

597 We annotated 143 raw and SoftWorx (Cytiva Life Sciences)-deconvolved FM 4-64 membrane
598 images using JFilament (Smith et al., 2010), as described above, yielding over 7000 cells for train-

ing. Training images were maximum-intensity projections of FM4-64 z-stacks. Following the Omnipose documentation (Cutler et al., 2022), we trained the models from scratch, i.e., not using any existing model parameters as starting points. In contrast, for Cellpose3 (Stringer & Pachitariu, 2025), Cellpose-SAM (Pachitariu et al., 2025) and microSAM (Archit et al., 2025), the existing base models were fine-tuned with the existing data. All trainings were done following the suggestions found in their respective documentations. Omnipose models were trained with a batch size of 8 images for 4000 epochs using a learning rate of 0.1 and a Rectified Adam (RAdam) optimizer (Liu et al., 2019). Both models (raw and deconvolved) were trained using the same parameters. Cellpose3 models were trained with a batch size of 1 image for 100 epochs using a learning rate of 0.1, a weight decay of $1x10^{-4}$, and a Stochastic Gradient Descent (SGD) optimizer (Sutskever et al., 2013). Both models (raw and deconvolved) were trained using the same parameters. Cellpose-SAM models were trained with a batch size of 1 image for 100 epochs using a learning rate of $1x10^{-5}$, a weight decay of 0.1, a tile size of 256x256 px, and an AdamW optimizer (Loshchilov & Hutter, 2017). Both models (raw and deconvolved) were trained using the same parameters. MicroSAM models were trained with a batch size of 1 image for 10 epochs of 1788 iterations per epoch, using a learning rate of $1x10^{-5}$, a weight decay of 0.1, a tile size of 512x512 px, and an AdamW optimizer. Segmentation decoder was also trained to allow for automatic instance segmentation. Both models (raw and deconvolved) were trained using the same parameters.

Training was done in the "deepbio" computing cluster at the Max Planck Institute for Evolutionary Biology, using a single NVIDIA(R) GeForce GTX 2080 Ti GPU with 12GB memory.

For accuracy assessment, we annotated 56 images with JFilament. F1 score (Caicedo et al., 2019; Maier-Hein et al., 2024; Taha & Hanbury, 2015) was calculated at eleven Intersection over Union (IoU) thresholds spanning 0.5 to 1, in 0.05 intervals. True positives, false positives, and false negatives were calculated using Omnipose library function "average_precision". F1 was then computed using these values following Caicedo et al. 2019 (Caicedo et al., 2019).

Simulation of fluorescent membranes

Synthetic rod-shaped cells were generated first by generating spheres of defined radii and then stretching them in the respective center point in the X-direction only. Contours were then obtained in each plane of each synthetic cell to mimic membranes. Contour spatial coordinates were extracted for simulating microscopy images using BlurLab (Ursell et al., 2017). For each contour

632 point, an intensity value was sampled from a normal distribution of mean 1000 and standard de-
633 viation 50. For simulating light spread, a Point-Spread Function (PSF) was simulated in BlurLab
634 using our image acquisition parameters: Numerical aperture of 1.4, refractive index of 1.518, emis-
635 sion wavelength of 679nm and magnification of 100X. Gaussian noise of mean 100 and standard
636 deviation 50 was added to the simulations. We then simulated Z-stacks of 4000 nm with 50 equi-
637 distant Z-slices for quantification.
638
639 **Training and evaluation of models for deconvolution prediction (FM2FM) and fluores-**
640 **cence translation (FP2FM)**
641 Deconvolution-prediction and fluorescence-translation models were trained using the Content
642 Aware Restoration (CARE) framework (Weigert et al., 2018). For FM2FM and FP2FM model,
643 200 images (2048x2048 pixels) of vegetatively growing *B. subtilis* constitutively expressing
644 mVenusQ69M (Cox et al., 2010) were acquired using a DeltaVision Ultra microscope with a PCO
645 Edge sCMOS camera, capturing FM4-64 membrane fluorescence, and mVenusQ69M cytoplasmic
646 fluorescence. Images were deconvolved in the DeltaVision software (SoftWorx) and then cropped
647 to remove deconvolution edge artifacts, yielding 1914x1914 px image outputs. Non-deconvolved
648 training inputs were cropped to the same size. Training input images were single-plane images of
649 raw FM4-64 (for the FM2FM model) or mVenusQ69M (for the FP2FM model) z-stacks, and
650 target images were the deconvolved FM4-64 images for both models. For training, 16 patches of
651 512x512 px were extracted from each image pair. Models were then trained using a batch size of
652 32 images for 100 epochs, with 100 training steps per epoch. Training was performed in the "deep-
653 bio" computing cluster at the Max Planck Institute for Evolutionary Biology, as above. Model
654 parameters and training hardware was the same for both models.
655
656 To compare model performance against the membrane deconvolution target (SoftWorx), we con-
657 ducted qualitative assessments of output images intensity profiles. We quantified the Structural
658 Similarity Index Measure (SSIM) between extracted patches of the images. Patches were selected
659 to maximize number of cells and minimize background. SSIM was calculated using the Python
660 scikit-image library (van der Walt et al., 2014). We then statistically compared cell-size estimates
661 using membrane images deconvolved with SoftWorx or predicted with FM2FM or FP2FM (Fig.
662 3; Supplementary Fig. 6). Width, Length, Surface Area, and Volume were measured using the
663 skeletons as explained further down. Cross-sectional area, convex hull area, eccentricity, and so-
664 lidity, were directly obtained from segmentation masks using the Python scikit-image library (van
665 der Walt et al., 2014).

666 **Training and evaluation of a deconvolution-prediction model that increases the signal-to-**
667 **noise ratio (SNR) of predicted images (FM2FM-HiSNR).**
668 We use CARE (Weigert et al., 2018) to train an additional deconvolution prediction model that
669 produces high signal-to-noise ratio (SNR) images from low SNR non-deconvolved fluorescent
670 membrane images. We named the model FM2FM-HiSNR. FM 4-64 images of vegetatively grow-
671 ing *B. subtilis* were acquired at four different illumination conditions using a DeltaVision Ultra
672 microscope with a PCO Edge sCMOS camera. The illumination conditions were as follows (ex-
673 posure time and percentage of transmitted light listed after their names in quotation marks):
674 "Noisy", 0.01s, 10%; "i1", 0.01s, 50%; "i2", 0.025s, 10%; "Target", 0.2s, 100%. Images were de-
675 convolved using the DeltaVision software (SoftWorx) and then cropped to remove deconvolution
676 edge artifacts, yielding 1914x1914 px image outputs. Non-deconvolved training inputs were
677 cropped to the same size. Training input images were single-plane images of raw FM4-64 z-stacks
678 from all different illumination conditions, and target images were the deconvolved FM4-64 images
679 at the "Target" illumination condition. In total, 98 input images were used. For training, 16 patches
680 of 512x512 px were extracted from each image pair. Model was then trained using a batch size of
681 32 images for 100 epochs, with 100 training steps per epoch. Training was performed in the "deep-
682 bio" computing cluster at the Max Planck Institute for Evolutionary Biology, as above.
683
684 To explore the relationship between SNR and segmentation accuracy, and to test whether resto-
685 ration with FM2FM-HiSNR improve segmentation accuracy of low SNR images, FM 4-64 images
686 of vegetatively growing *B. subtilis* were acquired at 12 different illumination conditions using a
687 DeltaVision Ultra microscope, under the following illumination conditions (exposure time and
688 percentage of transmitted light listed after their names in quotation marks): "Noisy", 0.01s, 10%;
689 "i1", 0.01s, 50%; "i2", 0.025s, 10%; "i3", 0.025s, 50%; "i4", 0.05s, 10%; "i5", 0.05s, 50%; "i6",
690 0.1s, 10%; "i7", 0.1s, 50%; "i8", 0.1s, 100%; "i9", 0.2s, 10%; "i10", 0.2s, 50%; "Target", 0.2s,
691 100%. Images were deconvolved using the DeltaVision software (SoftWorx) or restored with
692 FM2FM-HiSNR, and segmentation accuracy was calculated (Supplementary Fig. 13).
693
694 **Extracting cell size information from masks of rod-shaped cells.**
695 For rod-shaped bacteria, we assumed a sphero-cylindrical geometry with hemispherical caps (Ojkic
696 et al., 2019). First, we computed the minimum Euclidean distance from each pixel inside the mask
697 to the closest pixel on the mask boundary (Borgefors, 1986), which is commonly referred to as the
698 distance transform. Next, we generated a one-dimensional centerline (commonly known as "skel-

699 eton") (Zhang & Suen, 1984), overlaid it on the distance transform map, and determined the dis-
700 tance value at each skeleton pixel, thereby obtaining the local radius of the mask along the skeleton
701 line (Fig. 4a). An alternative one-dimensional representation is the medial axis (Blum, 1967), also
702 known as the "topological skeleton" (Supplementary Fig. 15). We compared size estimates ob-
703 tained with the two representations and found significant differences in some size metrics in a set
704 of *E. coli* cells (Supplementary Fig. 15d). Inspection of individual masks revealed that some medial-
705 axis representations tended to over-branch (Supplementary Fig. 15e). If common across many
706 cells, such over-branching would lead to inaccurate size estimates. We therefore proceeded with
707 the skeleton representation.
708
709 To estimate the extend of the hemispherical caps, we took the distance between each skeleton
710 endpoint and the corresponding mask tip as the cell radius at the skeleton endpoints. This yielded
711 precise estimates of mask length and with profiles at every pixel along the skeleton. Assuming
712 rotational symmetry and that the masks derive from medial focal-plane images, we estimated cell
713 volume and surface area by adding the volumes and lateral surface areas of cylindrical segments
714 generated by circularly projecting the radius of the mask at each pixel of the skeleton, plus the
715 hemispherical caps (Fig. 4a). This approach accurately handles elongated masks, provides local
716 morphological information of cell morphology, and is robust to cellular curvature. While tailored
717 to rods, the framework can be adapted to other morphologies.
718
719 *Dealing with branching skeletons*
720 Due to the mask geometry, it is possible that the skeleton branches into multiple endpoints (Sup-
721 plementary Fig. 15c). To handle both branched and non-branched cases, we developed the fol-
722 lowing workflow. First, we treat the skeleton as a graph, with each pixel considered a node. As-
723 suming connectivity only between neighboring pixels (horizontal, vertical, or diagonal), we define
724 edges for pairs of pixels whose Euclidean distance is less than 1.5 pixels, thereby retaining con-
725 nected neighbors. Next, we implement a Depth-first search (DFS) algorithm to find the longest
726 possible path connecting the opposite endpoints in the graph. If the skeleton is not branched, this
727 path corresponds to the skeleton. For branched skeletons, multiple candidate paths exist. For each
728 candidate path we compute the cell size metrics described in the next section and take the median
729 of each metric as the cell size (Supplementary Fig. 15).
730
731 *Cell size measurements:*

732 We combined the mask skeleton and distance transform to derive cell measurements under a
733 spherocylindrical geometry with hemispherical caps and rotational symmetry. The measurements
734 are implemented in a custom code written in Python3, which can be found in the GitHub reposi-
735 tory linked in the "Software and data availability section."
736
737 Cell length (L) is the sum of Euclidean distances d between two successive points in the mask
738 skeleton, plus the distance from each skeleton endpoint and the corresponding mask tip, which
739 corresponds to the local radius at the skeleton endpoint r_s. With that, L follows the equation:

740 $$L = r_{s1} + r_{s2} + \sum_{i=0}^{n-1} d(i,i+1). \qquad \text{Eq. (1)}$$

741 Cell width (w_i) is calculated as twice the value of the radius at each point in the skeleton (r_c). Mean
742 w can then be calculated as:

743 $$\bar{w} = \frac{2}{n} \sum_{i=0}^{n} r_{c\,i}. \qquad \text{Eq. (2)}$$

744 Cell surface area (S) is calculated as the sum of lateral surface areas of the cylinders projected at
745 each point in the skeleton, with radius r_c and height h of 1 pixel, plus the lateral surface area of
746 the hemispherical caps with radius r_s. Thus, S is calculated as:

747 $$S = 2\pi\,(r_{s1}^2 + r_{s2}^2 + h \sum_{i=0}^{n} r_{c\,i}). \qquad \text{Eq. (3)}$$

748 Cell volume (V) is obtained similarly to S, as it adds the volume of each cylinder and the hemi-
749 spherical caps (with same parameters of radius and height as S). V is then obtained from:

750 $$V = \pi(\frac{2}{3} r_{s1}^3 + \frac{2}{3} r_{s2}^3 + h \sum_{i=0}^{n} r_{c\,i}^2). \qquad \text{Eq. (4)}$$

751
752 **Measurement transformation**
753 We segmented 864 single cells of *Escherichia coli* stained with FM 4-64 using either JFilament
754 (ground-truth) or FMseg. Cells were from early exponential phase (OD_{600} = 0.1-0.3) cultures in
755 either LB Lennox, or MOPS minimal medium with 0.1% glucose, providing a range of cell widths
756 from 0.53 to 1.04 μm, and a range of cell lengths from 0.87 to 9.61 μm (based on measurements
757 from ground-truth masks) (Supplementary Figure 8a). Measurements from ground-truth masks
758 were plotted against the values obtained from on the FMseg-generated masks, revealing a con-
759 sistent size overestimation for FMseg masks (Supplementary Figure 8b). The data shows a linear
760 relationship for the overestimation, which allows us to leverage statistical tools to compute the

761 necessary parameters to transform the data between the automatic segmentation results to the
762 ground truth results. A linear regression would be a direct way to do this, extracting the values for
763 the slope (m) and intercept (n) necessary to transform the data. While linear regression returns a
764 coefficient of error that would allow us to simulate distributions to sample m and n, there is the
765 chance that we may over or under-estimate these values, as well as sample pairs that do not make
766 sense in the context of our data. Thus, we leveraged the PYMC library (Abril-Pla et al., 2023) and
767 its use of Bayesian statistics for sampling the necessary parameters, which are m, the fit slope, n,
768 the fit intercept, and σ, the standard deviation of our sampled observations. Since our data behaves
769 linearly, we used a Bayesian Generalized Linear Model (GLM), assuming that our parameters
770 (slope, intercept, size metric, and its standard deviation) follow certain types of distributions. For
771 σ, we assume a Half-Cauchy distribution, which only returns positive, non-zero values, which is
772 the only type of values a standard deviation can have. For m and n, we sample from normal distri-
773 butions with mean 0 and standard deviation 20, giving us a wide range of possible parameters.
774 Then, for computing the observed values, we also assume a normal distribution. PYMC performs
775 a series of draws to fit the data, and thus after successive draws we end with the distributions of
776 m, n and σ. In our case, we performed four chains of 3000 draws each, giving us a total of 12000
777 sampled values. We can then randomly sample pairs from these distributions in order to transform
778 the data, as well as to include the uncertainty of the transformation in the analysis (Supplementary
779 Figure 8b). For the examples shown in Figure 5, Figure 6, and Supplementary Figure 11, we sam-
780 pled 250 pairs of m and n for each individual cell measurement, thus allowing us to compute new
781 metrics.
782
783 **Statistical analyses**
784
785 For the statistical tests in Fig. 3, Fig. 6, Supplementary Fig. 6, and Supplementary Fig. 15, Levene's
786 test was computed for the distributions of interest. If the p value was greater than 0.05, one-way
787 ANOVA was performed for obtaining the p values and defining if the difference between distri-
788 butions was significant or not. In cases where Levene's test was significant ($p < 0.05$), Kruskal test
789 was used instead. All three tests were used as they are implemented in SciPy (Virtanen et al., 2020).
790
791 **CryoEM image analysis**
792 Because the high magnification of the cryo-EM images typically did not capture entire cells, we
793 estimated cell width as the straight-line distance between the mother-cell lateral membranes, meas-
794 ured perpendicular to the cell longitudinal axis. In cryo-FIB tomograms of wild-type cells, only a

795 portion of the cellular volume was retained: focused ion-beam milling produced a thin lamella that
796 sampled a section of the cell. We analyzed only tomograms in which this section included the mid-
797 cell region. To verify this, we measured width across successive z-slices and selected tomograms
798 showing a clear width peak at mid-cell that decreased in slices above and below.
799
800 **Whole genome sequencing**
801 For whole-genome sequencing, *Priestia megaterium* WH320 was streaked in an LB-Lennox agar plate
802 and grown overnight at 30°C. Next morning, a single colony was picked and re-streaked in an LB-
803 Lennox agar plate and grown overnight at 30°C. Cells were collected from the plate and genomic
804 DNA was extracted with the MasterPure Gram Positive DNA Purification Kit (Biosearch tech-
805 nologies). Extracted genome was then sequenced using an Illumina NextSeq 500 sequencer. Raw
806 pair-end sequences were loaded into Geneious prime version 2025.1.2 for sequence trimming and
807 pairing with an insert size of 500 base pairs. Paired sequence list was then exported in fastq format
808 for analysis using breseq (Deatherage & Barrick, 2014).
809
810 **Software and data availability**
811 The fine-tuned segmentation models for raw and deconvolved images (for Omnipose, Cellpose-
812 SAM, microSAM, and Cellpose3), deconvolution prediction (FM2FM), deconvolution prediction
813 and SNR increase (FM2FM-HiSNR2), and fluorescence translation (FP2FM) models can be found
814 in the Zenodo (https://zenodo.org/records/18978187). Segmentation model training and bench-
815 marking data can be found at the BioImage Archive repository https://www.ebi.ac.uk/biostud-
816 ies/studies/S-BIAD2350. Deconvolution model training and benchmarking data can be found at
817 the BioImage Archive repository https://www.ebi.ac.uk/biostudies/studies/S-BIAD2353. Im-
818 ages of individual *E. coli* cells used for measurement transformation with their corresponding an-
819 notations and automatic segmentations be found at the BioImage Archive repository
820 https://www.ebi.ac.uk/biostudies/studies/S-BIAD2352. Segmentation of *B. subtilis* and *P. mega-*
821 *terium* strains (wild-type and induction constructs) be found at the BioImage Archive repository
822 https://www.ebi.ac.uk/biostudies/studies/S-BIAD2354.
823 The MEDUSSA GitHub repository contains all software-related material
824 (https://github.com/OReyesMatte/MEDUSSA). The "MEDUSSA" folder contains the func-
825 tions for size measurement (measure.py), Bayesian sampling, and measurement transformation
826 (both in transform.py). The "CARE" folder contains the environment file which was used for
827 training the deconvolution models, as well as the corresponding notebooks for preparing the data,
828 train the model, and test it. The "Segmentation" folder contains the environment files for the

different segmentation frameworks, as well as examples for both training commands and uploading and running the models. The "Figures" folder contains notebooks to reproduce the plots shown in the manuscript. The "Raw data" folder contains all data used to make the manuscript plots. *P. megaterium* WH320 sequencing data, *ponA* protein sequence alignment, and results from breseq (Deatherage & Barrick, 2014) are available in Zenodo (https://zenodo.org/uploads/17392073).

ACKNOWLEDGMENTS

We are grateful to Elitza Tocheva, Elizabeth Villa and Kanika Khanna for kindly sharing CryoEM images of *B. subtilis* sporulating cells, Kaumudi H. Prabhakara for providing the *Saccharomyces cerevisiae* and *Lactococcus lactis* strains used in Fig. 2d, and Felipe Sinhorini for helping with the acquisition of the BGSC strains. We thank members of the Evolutionary Cell Biology group, the Ojkic lab, and the Microbial Population Biology department for continuous discussion and feedback. We thank Elisa Brambilla and Michael Schwarz for helping with the acquisition of images with the Zeiss Microscope. We also thank the members of the Scientific IT group at the Max Planck Institute for Evolutionary Biology for computational support. Work in JLG lab was supported by ERC starting grant 853323. NO was supported by BBSRC grant (BB/Y009002/1).

AUTHOR CONTRIBUTIONS

Conceptualization, ORM, NO, JLG; Methodology, ORM, JLG; Software, ORM, CFG, BG; Validation, ORM; Formal analysis, ORM, CFG, BG; Investigation, ORM, NH; Resources, NH; Data Curation, ORM; Writing - Original Draft, JLG; Writing - Review & Editing, All authors; Visualization, ORM, NO, JLG; Supervision, NO, JLG; Project administration, ORM, JLG; Funding acquisition, JLG.

COMPETING INTERESTS

The authors declare no competing interests.

REFERENCES

Abril-Pla, O., Andreani, V., Carroll, C., Dong, L., Fonnesbeck, C. J., Kochurov, M., Kumar, R., Lao, J., Luhmann, C. C., Martin, O. A., Osthege, M., Vieira, R., Wiecki, T., & Zinkov, R. (2023). PyMC: a modern, and comprehensive probabilistic programming framework in Python. *PeerJ Computer Science*, *9*, e1516. https://doi.org/10.7717/peerj-cs.1516

Agard, D. A. (1984). Optical sectioning microscopy: cellular architecture in three dimensions. *Annual Review of Biophysics and Bioengineering*, *13*, 191-219. https://doi.org/10.1146/annurev.bb.13.060184.001203

Archit, A., Freckmann, L., Nair, S., Khalid, N., Hilt, P., Rajashekar, V., Freitag, M., Teuber, C., Spitzner, M., Tapia Contreras, C., Buckley, G., von Haaren, S., Gupta, S., Grade, M., Wirth, M., Schneider, G., Dengel, A., Ahmed, S., & Pape, C. (2025). Segment Anything for Microscopy. *Nat Methods*, *22*(3), 579-591. https://doi.org/10.1038/s41592-024-02580-4

Arya, G., Petronella, N., Crosthwait, J., Carrillo, C. D., & Shwed, P. S. (2014). Draft genome sequence of *Bacillus megaterium* type strain ATCC 14581. *Genome Announcements*, *2*(6), e01124-01114. https://doi.org/10.1128/genomeA.01124-14

Bakshi, S., Leoncini, E., Baker, C., Canas-Duarte, S. J., Okumus, B., & Paulsson, J. (2021). Tracking bacterial lineages in complex and dynamic environments with applications for growth control and persistence. *Nat Microbiol*, *6*(6), 783-791. https://doi.org/10.1038/s41564-021-00900-4

Blum, H. (1967). A transformation for extracting new descriptors of shape. In W. Walthen-Dunn (Ed.), *Models for the Perception of Speech and Visual Form* (pp. 362-380). MIT Press.

Borgefors, G. (1986). Distance transformations in digital images. *Computer Vision, Graphics, and Image Processing*, *34*(3), 344-371. https://doi.org/https://doi.org/10.1016/S0734-189X(86)80047-0

Caicedo, J. C., Roth, J., Goodman, A., Becker, T., Karhohs, K. W., Broisin, M., Molnar, C., McQuin, C., Singh, S., Theis, F. J., & Carpenter, A. E. (2019). Evaluation of deep learning strategies for nucleus segmentation in fluorescence images. *Cytometry*, *95*(9), 952-965. https://doi.org/10.1002/cyto.a.23863

Calvez, P., Jouhet, J., Vie, V., Durmort, C., & Zapun, A. (2019). Lipid phases and cell geometry during the cell cycle of *Streptococcus pneumoniae*. *Frontiers in Microbiology*, *10*, 351. https://doi.org/10.3389/fmicb.2019.00351

Campos, M., Surovtsev, Ivan V., Kato, S., Paintdakhi, A., Beltran, B., Ebmeier, Sarah E., & Jacobs-Wagner, C. (2014). A constant size extension drives bacterial cell size homeostasis. *Cell*, *159*(6), 1433-1446. https://doi.org/10.1016/j.cell.2014.11.022

Chien, A. C., Hill, N. S., & Levin, P. A. (2012). Cell size control in bacteria. *Current Biology*, *22*(9), R340-R349. https://doi.org/10.1016/j.cub.2012.02.032

Cox, R. S., 3rd, Dunlop, M. J., & Elowitz, M. B. (2010). A synthetic three-color scaffold for monitoring genetic regulation and noise. *Joural of Biological Engineering*, *4*, 10. https://doi.org/10.1186/1754-1611-4-10

Cutler, K. J., Stringer, C., Lo, T. W., Rappez, L., Stroustrup, N., Brook Peterson, S., Wiggins, P. A., & Mougous, J. D. (2022). Omnipose: a high-precision morphology-independent solution for bacterial cell segmentation. *Nature Methods*, *19*(11), 1438-1448. https://doi.org/10.1038/s41592-022-01639-4

Cylke, A., & Banerjee, S. (2023). Super-exponential growth and stochastic size dynamics in rod-like bacteria. *Biophys J*, *122*(7), 1254-1267. https://doi.org/10.1016/j.bpj.2023.02.015

Dalebroux, Z. D., Edrozo, M. B., Pfuetzner, R. A., Ressl, S., Kulasekara, B. R., Blanc, M. P., & Miller, S. I. (2015). Delivery of cardiolipins to the *Salmonella* outer membrane is necessary for survival within host tissues and virulence. *Cell Host Microbe*, *17*(4), 441-451. https://doi.org/10.1016/j.chom.2015.03.003

de Bary, A. (1884). *Vergleichende Morphologie und Biologie der Pilze, Mycetozoen und Bacterien.* Engelmann.

Deatherage, D. E., & Barrick, J. E. (2014). Identification of mutations in laboratory-evolved microbes from next-generation sequencing data using breseq. *Methods in Molecular Biology*, *1151*, 165-188. https://doi.org/10.1007/978-1-4939-0554-6_12

Delaby, M., Yang, L., Jacq, M., Gallagher, K. A., Kysela, D. T., Hughes, V., Pulido, F., Veyrier, F. J., VanNieuwenhze, M. S., & Brun, Y. V. (2025). Phenotypic plasticity in cell elongation among closely related bacterial species. *Nature Communications*, *16*(1), 5099. https://doi.org/10.1038/s41467-025-60005-y

Dion, M. F., Kapoor, M., Sun, Y., Wilson, S., Ryan, J., Vigouroux, A., van Teeffelen, S., Oldenbourg, R., & Garner, E. C. (2019). *Bacillus subtilis* cell diameter is determined by the opposing actions of two distinct cell wall synthetic systems. *Nature Microbiology*, *4*(8), 1294-1305. https://doi.org/10.1038/s41564-019-0439-0

Dosovitskiy, A., Beyer, L., Kolesnikov, A., Weissenborn, D., Zhai, X., Unterthiner, T., Dehghani, M., Minderer, M., Heigold, G., & Gelly, S. (2020). An image is worth 16x16 words: Transformers for image recognition at scale. *arXiv preprint arXiv:2010.11929*.

Ducret, A., Quardokus, E. M., & Brun, Y. V. (2016). MicrobeJ, a tool for high throughput bacterial cell detection and quantitative analysis. *Nature Microbiology*, *1*(7), 16077. https://doi.org/10.1038/nmicrobiol.2016.77

Eppinger, M., Bunk, B., Johns, M. A., Edirisinghe, J. N., Kutumbaka, K. K., Koenig, S. S., Creasy, H. H., Rosovitz, M. J., Riley, D. R., Daugherty, S., Martin, M., Elbourne, L. D., Paulsen, I., Biedendieck, R., Braun, C., Grayburn, S., Dhingra, S., Lukyanchuk, V., Ball, B.,…Vary, P. S. (2011). Genome sequences of the biotechnologically important *Bacillus megaterium* strains QM B1551 and DSM319. *Journal of Bacteriology*, *193*(16), 4199-4213. https://doi.org/10.1128/JB.00449-11

Falk, T., Mai, D., Bensch, R., Cicek, O., Abdulkadir, A., Marrakchi, Y., Bohm, A., Deubner, J., Jackel, Z., Seiwald, K., Dovzhenko, A., Tietz, O., Dal Bosco, C., Walsh, S., Saltukoglu, D., Tay, T. L., Prinz, M., Palme, K., Simons, M.,…Ronneberger, O. (2019). U-Net: deep learning for cell counting, detection, and morphometry. *Nature Methods*, *16*(1), 67-70. https://doi.org/10.1038/s41592-018-0261-2

Gray, W. T., Govers, S. K., Xiang, Y., Parry, B. R., Campos, M., Kim, S., & Jacobs-Wagner, C. (2019). Nucleoid size scaling and intracellular organization of translation across bacteria. *Cell*, *177*(6), 1632-1648.e1620. https://doi.org/10.1016/j.cell.2019.05.017

Greenspan, P., & Fowler, S. D. (1985). Spectrofluorometric studies of the lipid probe, nile red. *Journal of lipid research*, *26*(7), 781-789. https://www.ncbi.nlm.nih.gov/pubmed/4031658

Gunawan, I., Marsh, R. J., Aggarwal, N., Meijering, E., Cox, S., Lock, J. G., & Culley, S. (2025). Image quality metrics fail to accurately represent biological information in fluorescence microscopy. *bioRxiv*, 2025.2008.2005.668508. https://doi.org/10.1101/2025.08.05.668508

Hardo, G., Li, R., & Bakshi, S. (2024). Quantitative microbiology with widefield microscopy: navigating optical artefacts for accurate interpretations. *Npj Imaging*, *2*(1), 26. https://doi.org/10.1038/s44303-024-00024-4

Herman, P., Konopasek, I., Plasek, J., & Svobodova, J. (1994). Time-resolved polarized fluorescence studies of the temperature adaptation in *Bacillus subtilis* using DPH and TMA-DPH fluorescent probes. *Biochimica et biophysica acta*, *1190*(1), 1-8. https://doi.org/10.1016/0005-2736(94)90028-0

Holt, J. H., Krieg, N. R., Sneath, P. H. a., Staley, J. T., & Williams, S. T. (1994). *Bergey's manual of determinative bacteriology ninth edition* (9th ed.). Lippincott Williams & Wilkins. https://doi.org/10.1016/j.ejpn.2008.10.006

Jiang, C., Caccamo, P. D., & Brun, Y. V. (2015). Mechanisms of bacterial morphogenesis: evolutionary cell biology approaches provide new insights. *BioEssays*, *37*(4), 413-425. https://doi.org/10.1002/bies.201400098

Juillot, D., Cornilleau, C., Deboosere, N., Billaudeau, C., Evouna-Mengue, P., Lejard, V., Brodin, P., Carballido-Lopez, R., & Chastanet, A. (2021). A high-content microscopy screening identifies new genes involved in cell width control in *Bacillus subtilis*. *mSystems*, *6*(6), e0101721. https://doi.org/10.1128/mSystems.01017-21

Kearns, D. B., & Losick, R. (2005). Cell population heterogeneity during growth of *Bacillus subtilis*. *Genes and Development*, *19*(24), 3083-3094. https://doi.org/10.1101/gad.1373905

Kellogg, D. R., & Levin, P. A. (2022). Nutrient availability as an arbiter of cell size. *Trends Cell Biol*, *32*(11), 908-919. https://doi.org/10.1016/j.tcb.2022.06.008

Khanna, K., Lopez-Garrido, J., Sugie, J., Pogliano, K., & Villa, E. (2021). Asymmetric localization of the cell division machinery during *Bacillus subtilis* sporulation. *eLife*, *10*, e62204. https://doi.org/10.7554/eLife.62204

Khanna, K., Lopez-Garrido, J., Zhao, Z., Watanabe, R., Yuan, Y., Sugie, J., Pogliano, K., & Villa, E. (2019). The molecular architecture of engulfment during *Bacillus subtilis* sporulation. *eLife*, *8*, e45257. https://doi.org/10.7554/eLife.45257

Kirillov, A., Mintun, E., Ravi, N., Mao, H., Rolland, C., Gustafson, L., Xiao, T., Whitehead, S., Berg, A. C., & Lo, W.-Y. (2023). Segment anything. Proceedings of the IEEE/CVF international conference on computer vision,

Kuru, E., Hughes, H. V., Brown, P. J., Hall, E., Tekkam, S., Cava, F., de Pedro, M. a., Brun, Y. V., & VanNieuwenhze, M. S. (2012). In Situ probing of newly synthesized peptidoglycan in live bacteria with fluorescent D-amino acids. *Angewandte Chemie (International ed. in English)*, *51*(50), 12519-12523. https://doi.org/10.1002/anie.201206749

Liu, L., Jiang, H., He, P., Chen, W., Liu, X., Gao, J., & Han, J. (2019). On the variance of the adaptive learning rate and beyond. *arXiv*, 1908.03265.

Logan, N. A., & Vos, P. D. (2015). *Bacillus*. In *Bergey's Manual of Systematics of Archaea and Bacteria* (pp. 1-163). https://doi.org/10.1002/9781118960608.gbm00530

López, A. C., & Alippi, A. M. (2009). Diversity of *Bacillus megaterium* isolates cultured from honeys. *LWT - Food Science and Technology*, *42*(1), 212-219. https://doi.org/10.1016/j.lwt.2008.05.001

Lopez-Garrido, J., Ojkic, N., Khanna, K., Wagner, F. R., Villa, E., Endres, R. G., & Pogliano, K. (2018). Chromosome translocation inflates *Bacillus* forespores and impacts cellular morphology. *Cell*, *172*(4), 758-770.e714. https://doi.org/10.1016/j.cell.2018.01.027

Loshchilov, I., & Hutter, F. (2017). Decoupled weight decay regularization. *arXiv preprint arXiv:1711.05101*.

Lucidi, M., Capecchi, G., Visaggio, D., Gasperi, T., Parisi, M., Cincotti, G., Rampioni, G., Visca, P., & Kolmakov, K. (2024). Expanding the microbiologist toolbox via new far-red-emitting dyes suitable for bacterial imaging. *Microbiology Spectrum*, *12*(1), e0369023. https://doi.org/10.1128/spectrum.03690-23

Lugagne, J. B., Lin, H., & Dunlop, M. J. (2020). DeLTA: Automated cell segmentation, tracking, and lineage reconstruction using deep learning. *PLoS Comput Biol*, *16*(4), e1007673. https://doi.org/10.1371/journal.pcbi.1007673

Lynch, M., Field, M. C., Goodson, H. V., Malik, H. S., Pereira-Leal, J. B., Roos, D. S., Turkewitz, A. P., & Sazer, S. (2014). Evolutionary cell biology: Two origins, one objective. *Proceedings of the National Academy of Sciences*, *111*(48), 16990-16994. https://doi.org/10.1073/pnas.1415861111

Ma, L., Conover, M., Lu, H., Parsek, M. R., Bayles, K., & Wozniak, D. J. (2009). Assembly and development of the *Pseudomonas aeruginosa* biofilm matrix. *PLoS Pathogens*, *5*(3), e1000354. https://doi.org/10.1371/journal.ppat.1000354

Maier-Hein, L., Reinke, A., Godau, P., Tizabi, M. D., Buettner, F., Christodoulou, E., Glocker, B., Isensee, F., Kleesiek, J., Kozubek, M., Reyes, M., Riegler, M. A., Wiesenfarth, M., Kavur, A. E., Sudre, C. H., Baumgartner, M., Eisenmann, M., Heckmann-Notzel, D., Radsch, T.,…Jager, P. F. (2024). Metrics reloaded: recommendations for image analysis validation. *Nature Methods*, *21*(2), 195-212. https://doi.org/10.1038/s41592-023-02151-z

Maloney, E., Madiraju, M., & Rajagopalan, M. (2009). Overproduction and localization of *Mycobacterium tuberculosis* ParA and ParB proteins. *Tuberculosis (Edinb)*, *89 Suppl 1*(Suppl 1), S65-69. https://doi.org/10.1016/S1472-9792(09)70015-0

Margulis, L., Jorgensen, J. Z., Dolan, S., Kolchinsky, R., Rainey, F. A., & Lo, S.-C. (1998). The *Arthromitus* stage of *Bacillus cereus:* Intestinal symbionts of animals. *Proceedings of the National Academy of Sciences*, *95*, 1236-1241.

Marks, M., Israel, U., Dilip, R., Li, Q., Yu, C., Laubscher, E., Iqbal, A., Pradhan, E., Ates, A., Abt, M., Brown, C., Pao, E., Li, S., Pearson-Goulart, A., Perona, P., Gkioxari, G., Barnowski, R., Yue, Y., & Van Valen, D. (2025). CellSAM: a foundation model for cell segmentation. *Nat Methods*, *22*(12), 2585-2593. https://doi.org/10.1038/s41592-025-02879-w

Monteiro, J. M., Fernandes, P. B., Vaz, F., Pereira, A. R., Tavares, A. C., Ferreira, M. T., Pereira, P. M., Veiga, H., Kuru, E., Vannieuwenhze, M. S., Brun, Y. V., Filipe, S. R., & Pinho, M. G. (2015). Cell shape dynamics during the staphylococcal cell cycle. *Nature Communications*, *6*, 1-12. https://doi.org/10.1038/ncomms9055

Murumkar, D. R., Borkar, S. G., & Chimote, V. P. (2012). Diversity for cell morphology, in-vitro phosphate solubilization and DNA profile of *Bacillus megaterium* isolates present in soils of Maharashtra. *World of Applied Sciences Journal*, *17*(6), 776-785.

Nordholt, N., van Heerden, J. H., & Bruggeman, F. J. (2020). Biphasic cell-size and growth-rate homeostasis by single *Bacillus subtilis* cells. *Current Biology*, *30*(12), 2238-2247 e2235. https://doi.org/10.1016/j.cub.2020.04.030

O'Connor, O. M., Alnahhas, R. N., Lugagne, J. B., & Dunlop, M. J. (2022). DeLTA 2.0: A deep learning pipeline for quantifying single-cell spatial and temporal dynamics. *PLoS Computational Biology*, *18*(1), e1009797. https://doi.org/10.1371/journal.pcbi.1009797

O'Hara, B. J., Barth, Z. K., McKitterick, A. C., & Seed, K. D. (2017). A highly specific phage defense system is a conserved feature of the *Vibrio cholerae* mobilome. *PLoS Genetics*, *13*(6), e1006838. https://doi.org/10.1371/journal.pgen.1006838

Ojkic, N., & Banerjee, S. (2021). Bacterial cell shape control by nutrient-dependent synthesis of cell division inhibitors. *Biophysical Journal*, *120*(11), 2079-2084. https://doi.org/10.1016/j.bpj.2021.04.001

Ojkic, N., López-Garrido, J., Pogliano, K., & Endres, R. G. (2014). Bistable forespore engulfment in *Bacillus subtilis* by a zipper mechanism in absence of the cell wall. *PLoS Computational Biology*, *10*(10), e1003912. https://doi.org/10.1371/journal.pcbi.1003912

Ojkic, N., López-Garrido, J., Pogliano, K., & Endres, R. G. (2016). Cell-wall remodeling drives engulfment during *Bacillus subtilis* sporulation. *eLife*, *5*, e18657. https://doi.org/10.7554/eLife.18657

Ojkic, N., Serbanescu, D., & Banerjee, S. (2019). Surface-to-volume scaling and aspect ratio preservation in rod-shaped bacteria. *eLife*, *8*, e47033. https://doi.org/10.7554/eLife.47033

Ojkic, N., Serbanescu, D., & Banerjee, S. (2022). Antibiotic resistance via bacterial cell shape-shifting. *mBio*, *13*(3), e0065922. https://doi.org/10.1128/mbio.00659-22

Ollion, J., Maliet, M., Giuglaris, C., Vacher, É., & Deforet, M. (2024). DiSTNet2D: Leveraging long-range temporal information for efficient segmentation and tracking. *PRX Life*, *2*(2), 023004. https://doi.org/10.1103/PRXLife.2.023004

Pachitariu, M., Rariden, M., & Stringer, C. (2025). Cellpose-SAM: superhuman generalization for cellular segmentation. *bioRxiv*, 2025.2004.2028.651001. https://doi.org/10.1101/2025.04.28.651001

Paintdakhi, A., Parry, B., Campos, M., Irnov, I., Elf, J., Surovtsev, I., & Jacobs-Wagner, C. (2016). Oufti: an integrated software package for high-accuracy, high-throughput quantitative microscopy analysis. *Molecular Microbiology*, *99*(4), 767-777. https://doi.org/10.1111/mmi.13264

Panigrahi, S., Murat, D., Le Gall, A., Martineau, E., Goldlust, K., Fiche, J. B., Rombouts, S., Nollmann, M., Espinosa, L., & Mignot, T. (2021). Misic, a general deep learning-based method for the high-throughput cell segmentation of complex bacterial communities. *eLife*, *10*, e65151. https://doi.org/10.7554/eLife.65151

Pogliano, J., Osborne, N., Sharp, M. D., Abanes-De Mello, a., Perez, a., Sun, Y. L., & Pogliano, K. (1999). A vital stain for studying membrane dynamics in bacteria: a novel mechanism controlling septation during *Bacillus subtilis* sporulation. *Molecular Microbiology*, *31*(4), 1149-1159.

Popham, D. L., & Setlow, P. (1996). Phenotypes of *Bacillus subtilis* mutants lacking multiple class A high-molecular-weight penicillin-binding proteins. *Journal of Bacteriology*, *178*(7), 2079-2085.

Riley, E. P., Trinquier, A., Reilly, M. L., Durchon, M., Perera, V. R., Pogliano, K., & Lopez-Garrido, J. (2018). Spatiotemporally regulated proteolysis to dissect the role of vegetative proteins during *Bacillus subtilis* sporulation: cell-specific requirement of σ^H and σ^A. *Molecular Microbiology*, *108*(1), 45-62. https://doi.org/10.1111/mmi.13916

Ronneberger, O., Fischer, P., & Brox, T. (2015). U-Net: Convolutional networks for biomedical image segmentation. In N. Navab, J. Hornegger, W. M. Wells, & A. F. Frangi, *Medical Image Computing and Computer-Assisted Intervention – MICCAI 2015* Cham.

Rygus, T., Scheler, A., Allmansberger, R., & Hillen, W. (1991). Molecular cloning, structure, promoters and regulatory elements for transcription of the *Bacillus megaterium* encoded regulon for xylose utilization. *Archives of Microbiology*, *155*(6), 526-534. https://doi.org/10.1007/BF00245346

Sauls, J. T., Cox, S. E., Do, Q., Castillo, V., Ghulam-Jelani, Z., & Jun, S. (2019). Control of *Bacillus subtilis* replication initiation during physiological transitions and perturbations. *mBio*, *10*(6), 10.1128/mbio.02205-02219. https://doi.org/10.1128/mBio.02205-19

Scalettar, B. A., Swedlow, J. R., Sedat, J. W., & Agard, D. A. (1996). Dispersion, aberration and deconvolution in multi-wavelength fluorescence images. *Journal of Microscopy*, *182*(1), 50-60. https://doi.org/10.1046/j.1365-2818.1996.122402.x

Schaechter, M., MaalOe, O., & Kjeldgaard, N. O. (1958). Dependency on Medium and Temperature of Cell Size and Chemical Composition during Balanced Growth of Salmonella typhimurium. *Journal of General Microbiology*, *19*(3), 592-606. https://doi.org/10.1099/00221287-19-3-592

Schavemaker, P. E., & Munoz-Gomez, S. A. (2022). The role of mitochondrial energetics in the origin and diversification of eukaryotes. *Nature Ecology and Evolution*, *6*(9), 1307-1317. https://doi.org/10.1038/s41559-022-01833-9

Schmidt, U., Weigert, M., Broaddus, C., & Myers, G. (2018). Cell detection with star-convex polygons. In A. F. Frangi, J. A. Schnabel, C. Davatzikos, C. Alberola-López, & G. Fichtinger, *Medical Image Computing and Computer Assisted Intervention – MICCAI 2018* Cham.

Schober, I., Koblitz, J., Sarda Carbasse, J., Ebeling, C., Schmidt, M. L., Podstawka, A., Gupta, R., Ilangovan, V., Chamanara, J., Overmann, J., & Reimer, L. C. (2025). BacDive in 2025: the core database for prokaryotic strain data. *Nucleic Acids Research*, *53*(D1), D748-D756. https://doi.org/10.1093/nar/gkae959

Sega, G. A. (1984). A review of the genetic effects of ethyl methanesulfonate. *Mutation Research*, *134*(2-3), 113-142. https://doi.org/10.1016/0165-1110(84)90007-1

Sharp, M. D., & Pogliano, K. (1999). An in vivo membrane fusion assay implicates SpoIIIE in the final stages of engulfment during *Bacillus subtilis* sporulation. *Proceedings of the National Academy of Sciences of the United States of America*, *96*(25), 14553-14558.

Shin, J. Y., Lopez-Garrido, J., Lee, S.-H. H., Diaz-Celis, C., Fleming, T., Bustamante, C., & Pogliano, K. (2015). Visualization and functional dissection of coaxial paired SpoIIIE channels across the sporulation septum. *eLife*, *4*(MAY), e06474. https://doi.org/10.7554/eLife.06474

Smith, M. B., Li, H., Shen, T., Huang, X., Yusuf, E., & Vavylonis, D. (2010). Segmentation and tracking of cytoskeletal filaments using open active contours. *Cytoskeleton*, *67*(11), 693-705. https://doi.org/10.1002/cm.20481

Spahn, C., Gomez-de-Mariscal, E., Laine, R. F., Pereira, P. M., von Chamier, L., Conduit, M., Pinho, M. G., Jacquemet, G., Holden, S., Heilemann, M., & Henriques, R. (2022). DeepBacs for multi-task bacterial image analysis using open-source deep learning approaches. *Communications Biology*, *5*(1), 688. https://doi.org/10.1038/s42003-022-03634-z

Specht, M., Dempwolff, F., Schatzle, S., Thomann, R., & Waidner, B. (2013). Localization of FtsZ in *Helicobacter pylori* and consequences for cell division. *Journal of Bacteriology*, *195*(7), 1411-1420. https://doi.org/10.1128/JB.01490-12

Stahl, U., & Esser, K. (1983). Plasmid heterogeneity in various strains of *Bacillus megaterium*. *European journal of applied microbiology and biotechnology*, *17*(4), 248-251. https://doi.org/10.1007/BF00510424

Strahl, H., Burmann, F., & Hamoen, L. W. (2014). The actin homologue MreB organizes the bacterial cell membrane. *Nat Commun*, *5*, 3442. https://doi.org/10.1038/ncomms4442

Stringer, C., & Pachitariu, M. (2025). Cellpose3: one-click image restoration for improved cellular segmentation. *Nature Methods*, *22*(3), 592-599. https://doi.org/10.1038/s41592-025-02595-5

Stringer, C., Wang, T., Michaelos, M., & Pachitariu, M. (2021). Cellpose: a generalist algorithm for cellular segmentation. *Nature Methods*, *18*(1), 100-106. https://doi.org/10.1038/s41592-020-01018-x

Studer, P., Staubli, T., Wieser, N., Wolf, P., Schuppler, M., & Loessner, M. J. (2016). Proliferation of *Listeria monocytogenes* L-form cells by formation of internal and external vesicles. *Nature Communications*, *7*, 13631. https://doi.org/10.1038/ncomms13631

Stylianidou, S., Brennan, C., Nissen, S. B., Kuwada, N. J., & Wiggins, P. A. (2016). SuperSegger: robust image segmentation, analysis and lineage tracking of bacterial cells. *Molecular Microbiology*, *102*(4), 690-700. https://doi.org/10.1111/mmi.13486

Sun, Q., & Margolin, W. (1998). FtsZ dynamics during the division cycle of live *Escherichia coli* cells. *Journal of Bacteriology*, *180*(8), 2050-2056. https://doi.org/10.1128/JB.180.8.2050-2056.1998

Sutskever, I., Martens, J., Dahl, G., & Hinton, G. (2013). *On the importance of initialization and momentum in deep learning* Proceedings of the 30th International Conference on Machine Learning, Proceedings of Machine Learning Research.

Syvertsson, S., Vischer, N. O., Gao, Y., & Hamoen, L. W. (2016). When phase contrast fails: ChainTracer and NucTracer, two ImageJ methods for semi-automated single cell analysis using membrane or DNA staining. *PLoS ONE*, *11*(3), e0151267. https://doi.org/10.1371/journal.pone.0151267

Taha, A. A., & Hanbury, A. (2015). Metrics for evaluating 3D medical image segmentation: analysis, selection, and tool. *BMC Medical Imaging*, *15*, 29. https://doi.org/10.1186/s12880-015-0068-x

1159 Taheri-Araghi, S., Bradde, S., Sauls, J. T., Hill, N. S., Levin, P. A., Paulsson, J., Vergassola, M., &
1160 Jun, S. (2015). Cell-size control and homeostasis in bacteria. *Current Biology*, *25*(3), 385-
1161 391. https://doi.org/10.1016/j.cub.2014.12.009
1162 Tocheva, E. I., López-Garrido, J., Hughes, H. V., Fredlund, J., Kuru, E., Vannieuwenhze, M. S.,
1163 Brun, Y. V., Pogliano, K., & Jensen, G. J. (2013). Peptidoglycan transformations during
1164 *Bacillus subtilis* sporulation. *Molecular Microbiology*, *88*(4), 673-686.
1165 https://doi.org/10.1111/mmi.12201
1166 Tsuge, Y., Ogino, H., Teramoto, H., Inui, M., & Yukawa, H. (2008). Deletion of cgR_1596 and
1167 cgR_2070, encoding NlpC/P60 proteins, causes a defect in cell separation in
1168 *Corynebacterium glutamicum* R. *Journal of Bacteriology*, *190*(24), 8204-8214.
1169 https://doi.org/10.1128/JB.00752-08
1170 Ursell, T., Lee, T. K., Shiomi, D., Shi, H., Tropini, C., Monds, R. D., Colavin, A., Billings, G.,
1171 Bhaya-Grossman, I., Broxton, M., Huang, B. E., Niki, H., & Huang, K. C. (2017). Rapid,
1172 precise quantification of bacterial cellular dimensions across a genomic-scale knockout
1173 library. *BMC Biology*, *15*(1), 17. https://doi.org/10.1186/s12915-017-0348-8
1174 van der Walt, S., Schonberger, J. L., Nunez-Iglesias, J., Boulogne, F., Warner, J. D., Yager, N.,
1175 Gouillart, E., Yu, T., & scikit-image, c. (2014). scikit-image: image processing in Python.
1176 *PeerJ*, *2*, e453. https://doi.org/10.7717/peerj.453
1177 Van Valen, D. A., Kudo, T., Lane, K. M., Macklin, D. N., Quach, N. T., DeFelice, M. M.,
1178 Maayan, I., Tanouchi, Y., Ashley, E. A., & Covert, M. W. (2016). Deep learning
1179 automates the quantitative analysis of individual cells in live-cell imaging experiments.
1180 *PLoS Computational Biology*, *12*(11), e1005177.
1181 https://doi.org/10.1371/journal.pcbi.1005177
1182 Virtanen, P., Gommers, R., Oliphant, T. E., Haberland, M., Reddy, T., Cournapeau, D.,
1183 Burovski, E., Peterson, P., Weckesser, W., Bright, J., van der Walt, S. J., Brett, M.,
1184 Wilson, J., Millman, K. J., Mayorov, N., Nelson, A. R. J., Jones, E., Kern, R., Larson,
1185 E.,…SciPy, C. (2020). SciPy 1.0: fundamental algorithms for scientific computing in
1186 Python. *Nat Methods*, *17*(3), 261-272. https://doi.org/10.1038/s41592-019-0686-2
1187 Weigert, M., Schmidt, U., Boothe, T., Muller, A., Dibrov, A., Jain, A., Wilhelm, B., Schmidt, D.,
1188 Broaddus, C., Culley, S., Rocha-Martins, M., Segovia-Miranda, F., Norden, C.,
1189 Henriques, R., Zerial, M., Solimena, M., Rink, J., Tomancak, P., Royer, L.,…Myers, E.
1190 W. (2018). Content-aware image restoration: pushing the limits of fluorescence
1191 microscopy. *Nature Methods*, *15*(12), 1090-1097. https://doi.org/10.1038/s41592-018-
1192 0216-7
1193 Yeh, Y. C., Comolli, L. R., Downing, K. H., Shapiro, L., & McAdams, H. H. (2010). The
1194 *Caulobacter* Tol-Pal complex is essential for outer membrane integrity and the positioning
1195 of a polar localization factor. *Journal of Bacteriology*, *192*(19), 4847-4858.
1196 https://doi.org/10.1128/JB.00607-10
1197 Zhang, T. Y., & Suen, C. Y. (1984). A fast parallel algorithm for thinning digital patterns.
1198 *Communications of the ACM*, *27*(3), 236–239. https://doi.org/10.1145/357994.358023
1199 Zou, X., Yang, J., Zhang, H., Li, F., Li, L., Wang, J., Wang, L., Gao, J., & Lee, Y. J. (2023).
1200 Segment everything everywhere all at once. *Advances in neural information processing systems*,
1201 *36*, 19769-19782.

1202